Mechanism and application of morphological changes of Si crystal material induced by ion-beam

Jianguo Zhang

1138005

Department of Mechanical Systems Engineering,

Kochi University of Technology

September, 2012

Abstract:

The fabrication technique of 3-D micro/nano structure is a hopeful technique used in electric device, micro-electromechanical, optical device and biochip, etc. In this thesis, we study controlling vertical level of 3-D nano structure by fabrication swelling (positive level) and crater structures (negative level) method.

It has been found that ion irradiation can induce a swelling (step-height) phenomenon on crystal surface. In this thesis, we studied about the control of swelling height of Si crystal by irradiating Ar beam under various irradiation parameters (fluence, charge and energy). These irradiation parameters were regulated by an irradiation facility that enables to achieve the multiple ionization. For the charges depenence, the swelling height was studied with the various fluence of two different charges Ar^{1+} and Ar^{4+}. The swelling height increased with increasing the fluence. The swelling height was also studied by changing energy of Ar^{4+} beam. The swelling height increased by increasing the energy. The obtained swelling heights are understood base on the contribution of ion-beam induced defect, which is evaluated by SRIM. By comparing with the previous results, it was found that the expansion phenomena also depend on atomic number of irradiated ion. And, the swelling structures fabricated in the present were found to be stable more than two months.

The swelling phenomenon and its morphological change through the thermal annealing process of Si crystal, irradiated by Ar^{+} and C^{+} beams have been studied. The height of swelling structures produced by the Ar^{+} beam is much higher than that

produced by the C^+ beam at energy 90 keV with the fluence up to 8 - 10^{16}/cm^2. The large difference in the swelling height was well understood base on the productivity of vacancies evaluated by the SRIM simulation and experiment. Post- irradiation samples irradiated with fluence 4 - 10^{16}/cm^2, were annealed at various temperatures in the range of 200 – 800 ℃. In the case of Ar^+ irradiated samples, the swelling height started to increase at about 600 ℃. In contrast, in the case of C^+ beam irradiated samples, the swelling height started to decrease at about 600 ℃ and almost disappeared at 800 ℃. The opposite behavior is understood based on the difference in irradiation-induced defect and in rearrangement mechanism in the thermal annealing process.

The silicon swelling structure has also been successfully fabricated on Si surface by heavy ion - Kr ion with fluence of 0.5×10^{15} ～ 8×10^{16} atoms/cm^2. The swelling height increases with the fluence increasing as for Ar-beam. After irradiation, the irradiated samples were annealed with temperature range 200 ～ 800 ℃. The swelling heights show different features corresponding to the fluence of Kr beam. In order to understand, this difference by evaluating damage in the Si target. The Raman spectroscopy is used to measure the samples. For the irradiated samples, crystal Si peak (520 cm^{-1}) disappears and the amorphous Si peak arises. After annealed at 600 ℃, the amorphous Si is recrystal. The surface morphology was studied by the sample of irradiated by 8×10^{16} atoms/cm^2.

The fabrication process of crater structures on Si crystal has been studied by an irradiation of Ar beam and a thermal annealing at 600 ℃. The fabricated surface was

measured by field emission scanning electron microscope and atomic force microscope. The results have shown the controllability of specifications of crater formation such as density, diameter and depth by changing two irradiation parameters - fluence and energy of Ar ions. By changing the fluence over a range of $1 \sim 10 \times 10^{16}/cm^2$, we could control a density of crater $0 \sim 39$ counts/100μm^2. By changing the energy over a range of 90 ~ 270 keV, we could control a diameter and a depth of crater in 0.8 ~ 4.1 μm and 99 ~ 229 nm, respectively. The present result is consistent with the previously proposed model that the crater structure would be arising from an exfoliated surface layer of silicon. The present result has indicated the possibility of the crater production phenomena as a hopeful method to fabricate the surface pattern on a micro-nano meter scale.

Based on the above results, it is proved that these methods of producing swelling structure and crater structure indicate the potential application to fabricate 3-D nanostructure.

1. Introduction ········· *8*

1.1 Swelling phenomenon and possibility in micro/nanoscale fabrication ········· **9**

1.2 Surface pattern and possibility in the crater surface patterning ········· **11**

2. Fundamental theory ········· *13*

2.1 Silicon crystal ········· **13**

2.2 Nuclear and Electronic damage ········· **16**

2.2.1 Damage induced in materials by ion irradiation: ········· 19

2.2.2 Sputtering: ········· 20

2.3 Annealing effect ········· **22**

3. Experimental method ········· *24*

3.1 Preparation of Si samples ········· **24**

3.2 Irradiation of ion beam onto crystal silicon ········· **24**

3.3 Thermal annealing ········· **27**

3.4 Techniques for sample evalution ········· **28**

3.4.1 Alpha-Step IQ Surface Profiler (KLA-Tencor Corporation) ········· 28

3.4.2 Atomic force microscopy ········· 32

3.4.3 Scanning electron microscopy measurement and mechanism ········· 33

3.4.4 Raman spectroscopy ········· 34

3.4.5 Transmission Electron Microscope (TEM) ········· 36

3.4.6 Simulation of irradiation effect by means of SRIM ········· 39

Chapter 4. Control of Swelling Height of Si Crystal by Irradiating Ar Beam ········· *41*

4.1 Definition of the swelling height ········· **41**

4.2 The fluence dependence ········· **42**

4.3 The energy dependence ········· **45**

4.4. Comparison with the simulation ········· **46**

4.5 Stability of swelling structure at room temperature ········· **51**

Chapter 5. Swelling and annealing phenomena of Si crystal irradiated by Ar and C ion beams ········· *52*

5.1 Comparison of Si swelling height produced by Ar and C beams ········· **52**

5.2 Simulation of ········· **53**

5.3 Modification induced by thermal annealing ········· **56**

Chapter 6. Experimental study on the mechanism of Si swelling phenomenon by Kr beam ········· *61*

6.1 Swelling effects induce by Kr beam irradiation ········· **61**

6.2 Annealing results ········· **63**

6.3 Modification of lattice structure of Si crystal observed by Raman spectroscopy 65

6.4 Modification of the surface roughness induced by annealing process ················ 68

Chapter 7. Fabrication of Si surface pattern by Ar beam irradiation and annealing method ··· ***71***

7.1 Definition of the crater structure ··· 71

7.2 Fluence dependence ··· 72

7.3 Energy dependence ··· 75

7.4 The comparison with previous data ··· 81

8. Conclusion ··· ***86***

Acknowledgement: ··· ***90***

References: ··· ***91***

List of acronyms

AFM – Atomic force microscopy (or microscope)

BF – Bright-field

TEM – Transmission electron microscopy

HEMT – High electron mobility transistor

SEM – Scanning electron microscopy (microscope)

RT – Room-temperature

RMS – Root mean square

SRIM – the Stopping and Range of Ions in Matter

1. Introduction

Micro/nanoscale fabrication techniques for semiconductor materials, are necessary in various industrial fields, such as microelectromechanical systems (MEMS) and nanoelectromechanical systems (NEMS), optical device and biochip, etc. These devices are fabricated by semiconductor materials, such as silicon (Si), germanium (Ge), silicon carbide (SiC) and gallium arsenide (GaAs), etc.

In the conventional methods, fabrication of 2 - dimensional structures is used in electric device. Next generation 2 - dimensional structure is concentration on high density and small size. Now, the hopeful structures in 3 - dimensional structure (MEMS, NIMS) can be use not only electric device but also mechanical, optical and biochip, etc.

Photolithography is the standard and mature process used to fabricate micro/nanoscale structures [1, 2], which can produce structures with a minimum line width of less than 1 μm. This method is suitable for mass-producing structures because it allows high-throughput fabrication. However, it is necessarily involved multiple steps: 1) patterning of a resist layer by ultraviolet light with optical masks And 2) fabrication of structures using subsequent wet or dry etching processes.

Ion beam method has been known also a powerful tool for the fabrication of structures on materials surface, and has been used in various industrial fields in recent years, such as ion beam milling [3], ion beam deposition [4] and ion beam irradiation connecting with wet chemical etching [5] they are the widely used

techniques [6]. The ion milling method needs to high fluence (typically $\Phi \leqq 10^{18}/cm^2$) and long time irradiation [7]. The ion beam deposition method often uses the focused ion beam assisted deposition or ion beam sputtering method assisted deposition. The ion beam irradiation connecting with wet chemical etching method need several steps and complex processes [5].

Some researchers have successfully fabricated 3 - dimensional structures with traditional methods, but controllability of the vertical direction and simple and controllable method is the open question. Recently, some researchers have discovered the irradiated region lifts up after ion beam irradiation [8-13] - the swelling phenomenon. This is a simple and controllable method for the 3 - dimensional micro/nanoscale fabrication techniques in vertical (up) direction. On the other hand, some researcher have studied the surface pattern of the crater can be fabricated by annealing the irradiated semiconductor sample [14-17]. This method can be used to fabricate large areas and controllable 3 - dimensional crater surface patterns in vertical (down) direction.

The details of these new methods will be advocated below:

1.1 Swelling phenomenon and possibility in micro/nanoscale fabrication

Ion beam irradiation method is one of the popular methods to modify the property of materials. The irradiation with energetic ion beams induces considerable structural

and chemical modification leading to a change of mechanical, electric, optical, and thermal properties, etc. The example of change in morphology is surface swelling [18, 8], etc. The swelling phenomenon has been obtained in a great number of different semiconductors and insulators such as Si, Ge, SiC, GaAs, GaN, MgO, $LiNbO_3$, Al_2O_3, LiF, etc. The behaviors of these swelling processes strongly depend on the materials and irradiation parameters: ion mass, fluence, energy, dwell time, incident angle etc [19, 20]. The previous studies has shown that the swelling phenomena are mainly contributed by amorphization of the target [11, 21], while the irradiation ion forms a limited contribution to the surface expansion [10]. The amorphization induces the volume expansion and the decrease in density of the bombarded regions [8], which lead to the swelling effect. The studies in the amorphized regions of Ge [22] and GaSb [23] discovered the formation of nanopores or voids as responsible for the volume expansion in the irradiated region, but such structure were not found in our experimental target [24].

Silicon is one of popular materials in semiconductor industry, while most of the swelling effects of Si were investigate by the host ion beam [10, 11, 25]. However, the Si swelling effect is rarely studied by irradiating inpurity ions, especially rare gas ions. According to the previous studies, the swelling height is mainly explained by irradiation induced defect, which makes transformation from crystalline silicon to amorphous silicon after ion beam irradiation [26-29]. Considering the heavier mass, larger radius and stability of rare gas ions, the Ar and Kr ions are employed in the present experiment. In this work, we studied the swelling phenomenon of Si crystal

by irradiating Ar and Kr beams and then relax the irradiated samples through annealing method at high temperature.

1.2 Surface pattern and possibility in the crater surface patterning

The surface pattern has an extensive application in many fields, such as semiconductor device [30], photonics [31], biosensors [32], and biochip, etc. Using ion beam method to form the surface pattern are widely applied by the ion beam lithography [33-35] and focused ion beam method. The ion beam lithography method is necessarily involved multiple steps and high irradiation fluence. The focused ion beam method can fabricate fine and precise surface patterns, but it fails to fabrication in large areas.

The smart-cut technical has been designed by Bruel [36] in 1995 incorporates four steps: H ion irradiation, cleaning - wafer bonding, heat treatment (fracture to transfer a thin layer) and polishing. Recently, some studies has concentrated on a part of the smart-cut technical, ion irradiation and heat treatment, as a simple method to fabricate surface patterns (blister and crater). Huang *et al.* [37] studied the surface blister process by hydrogen irradiation. Wang *et al.* [38] reported surface exfoliation phenomenon by helium and hydrogen co-irradiation. Markwitz *et al.* [14] presented formation of crater structure by neon irradiation and electron beam annealing. The fabrications often have been performed by irradiation hydrogen or rare gas ion. The irradiated hydrogen atom introduces the chemical bond in Si crystal [39], and the

property of the target may change. The rare gas ion beam irradiation and annealing method, that induce less modification of target comparing with other elements, is a hopeful method to fabricate the large area surface pattern. However the knowledge to control the surface pattern is still poor.

In this research, we realize the fabrication of crater surface patterns by using argon beam on Si target, also we study the fluence and energy dependence to control the specific fabrication. The advantage of this method is that there is no chemical interaction in silicon substrate as Ar atoms, but it performs as physical interaction just as hydrogen does or even more efficiently. The mechanism of forming the crater will also be discussed.

2. Fundamental theory

In order to explain, the basic knowledge of this study, following points will be explained in this section.

- Silicon crystal
- Electronic and nuclear damage
- Annealing effect

Lattice order

Damage disorder → Expansion, Stress

Relaxation order → Expansion, Stress

2.1 Silicon crystal

Silicon is one of the elements in Group IV of the periodic table. Electron configuration of silicon is shown in fig. 2-1. 14 electrons occupy the 3 energy levels $1s^2$, $2s^2 2p^6$, and $3s^2$ $3p^2$. Silicon shows the semiconductor property. A semiconductor has electrical conductivity intermediate in magnitude between a conductor and an insulator. Owing to these properties [40], decide silicon crystal has become the most widely used semiconductor materials in the market.

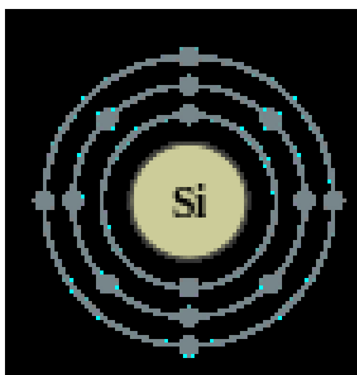

Figure. 2-1 Electron configuration of silicon atom

The silicon crysrtal is produced either by the Czochralski crystal (CZ) pull method or by the floating-zone crystal (FZ) growth technique. Impurities (dopants) are added to the silicon in order to set the resistivity of the wafer in a range from 0.1 Ωcm - 50 Ωcm. On the other hand an epitaxial layer (same crystal structure as the underlying wafer) is often grown on the substrate by a high temperature CVD process. These epitaxial layers are used to form buried layers or to put a lightly doped layer on top of a heavily doped substrate.

Crystal Planes and Miller Indices:

Since actual crystals are not infinitely large, they eventually terminate at a surface. Surfaces, or planes through the crystal, can be defined by first considering the intercepts of the plane along the *X, Y,* and *Z* axes used to describe the lattice, as shown in Figure 2.2.

In case of the figure, the intercepts of the plane correspond to $X=2$, $Y=3$ and $Z=1$. Now write the reciprocals of the intercepts, which gives

$$\left(\frac{1}{2},\frac{1}{3},\frac{1}{1}\right)$$

Multiply by the lowest common denominator, which in this case is 6, to obtain (3, 2, 6). The plane, shown in Fig 2-2, is then referred to as the (326) plane. The integers are referred to as the Miller indices. We will refer to a general plane as the (*hkl*) plane.

We can show that the same three Miller indices are obtained for any plane that is

parallel to the one shown in Figure 2.2.

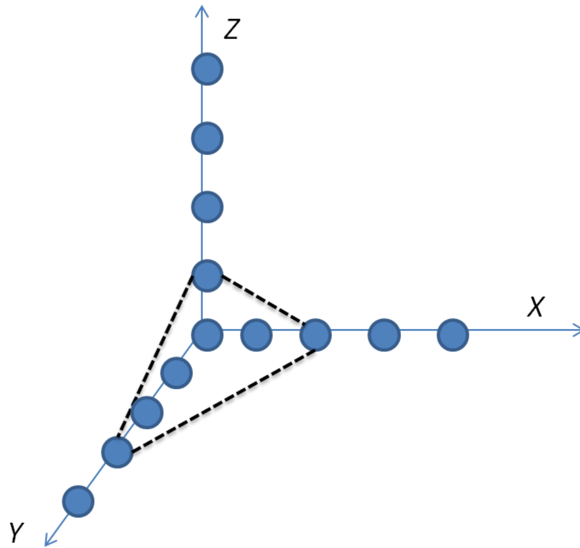

Figure 2-2 Definition of crystal lattice plane by means of intercepts.

For example, three planes that are commonly considered in a cubic crystal are shown in Figure 2-3. The plane in Figure 2-3(a) is parallel to the *Y* and *Z* axes so the intercepts are given as $X=1,\ Y=\infty,\ and\ Z=\infty$. According to the definition of miller indices the plane shown in Figure 2-3(a) is referred to as the (100) plane. Again, any plane parallel to the one shown in Figure 2-3(a) and separated by an integral number of lattice constants is equivalent and is referred to as the (100) plane. One advantage to taking the reciprocal of the intercepts to obtain the Miller indices is that the use of infinity is avoided when describing a plane that is parallel to an axis. If we were to describe a plane passing through the origin of our system, we would obtain infinity as one or more of the Miller indices after taking the reciprocal of the intercepts. However, the location of the origin of our system is entirely arbitrary and so, by

translating the origin to another equivalent lattice point, we can avoid the use of infinity in the set of Miller indices.

In case of Figure 2-3(b), the intercepts of the plane are *X=1, Y=1* and *Z=0*, and this plane is referred to as the (110) plane. In a similar way, the plane shown in Figure 2.3(c) is referred to as the (111) plane

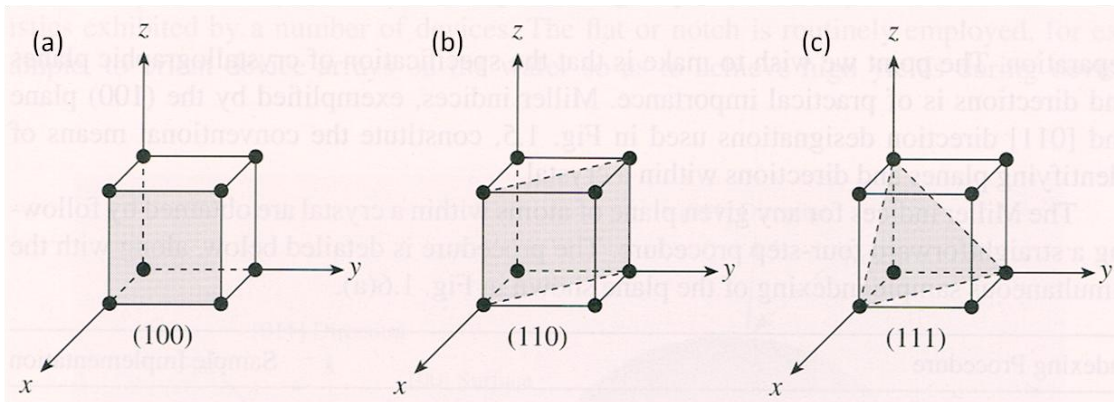

Figure 2-3 Three lattice planes in simple cubic lattice: (a) (100) plane, (b) (110) plane, (c) (111) plane

2.2 Nuclear and Electronic damage

When an energetic ion penetrates a solid, the ion undergoes a series of collisions with the atoms and electrons in the solid. In these collisions, the incident particle losses energy, depending on the energy and mass of the ion as well as on the substrate material. The concerned with the penetration depth, range *R*, of ions:

$$R=\int_{E_0}^{0} \frac{1}{dE/dx}\, dE$$

(1)

When E_0 is the incident energy of the ion as it penetrates the solid. The sign of dE/dx is negative as it represents the energy loss per increment of path, although tabulated values are given as positive quantities. The distribution is referred to as the range distribution or range straggling. In case of ion irradiation, it is not the total distance *R* traveled by the ion that is of interest but the projection of *R* normal to the surface.

The energy-loss process:

The energy loss rate dE/dx of an energetic ion moving through a solid is determined by screened Coulomb interaction with the substrate atoms and electrons. It is usually separated into two different mechanism of energy loss: (1) nuclear collision, in which energy is transmitted as translator motion to a target atom as a whole, and (2) electronic collisions, in which the moving particle excites or ejects atomic collisions. For most purpose, this separation into elastic and inelastic collisions is a convenient one and, although not strictly true, it is a good approximation. According to this idea, energy loss rate dE/dx can be expressed as:

$$\frac{\mathrm{d}E}{\mathrm{d}x} = \left.\frac{\mathrm{d}E}{\mathrm{d}x}\right|_{\mathrm{n}} + \left.\frac{\mathrm{d}E}{\mathrm{d}x}\right|_{\mathrm{e}} \tag{2}$$

where the subscripts *n* and *e* denote nuclear and electronic collisions, respectively.

Nuclear collision can involve large discrete energy losses and significant angular deflection of the trajectory of the ions as shown in fig. 2-4. This process is responsible for the production of lattice disorder by the displacement of atoms from

their positions of lattice. Electronic collisions also cause energy losses, but the contribution is smaller than nuclear collision per collision. Therefore,electronic collision induces negligible deflection of the ion trajectory and lattice disorder. The relative importance of the two energy loss process strongly depend on changes rapidly with energy *E* and atomic number *Z* of the ions: Nuclear stopping predominates for low *E* and high *Z*, whereas electronic take over for high *E* and low *Z*. Electron-volt per nanometer or kilo-electron-volt per micrometer are used as a mount of the energy loss rate. In this research, nuclear collisions are dominant compared with electronic collisions.

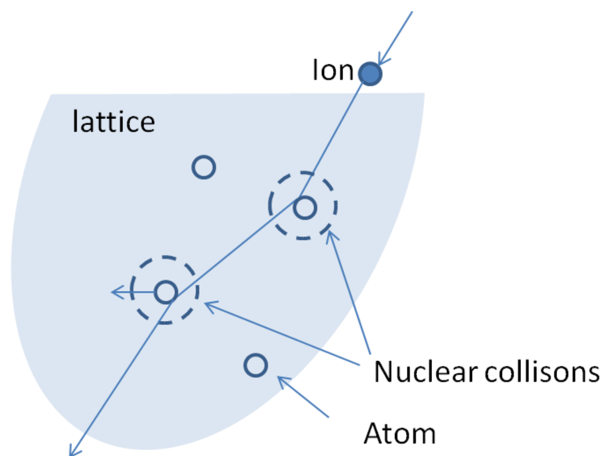

Figure 2-4 Collision of incident ion in material. The orbit of ion is deflected by nuclear collisions with lattice atoms, and also loses energy in collisions with electrons.

2.2.1 Damage induced in materials by ion irradiation:

While an energetic ion passes through a material, it loses energy through both of nuclear and electronic conditions. When an ion with initial energy *E* travels through a thin segment d*x* of the thick target, it is possible for the ion to experience a collision with a lattice atom, an electron or no collision in Fig 2-5.

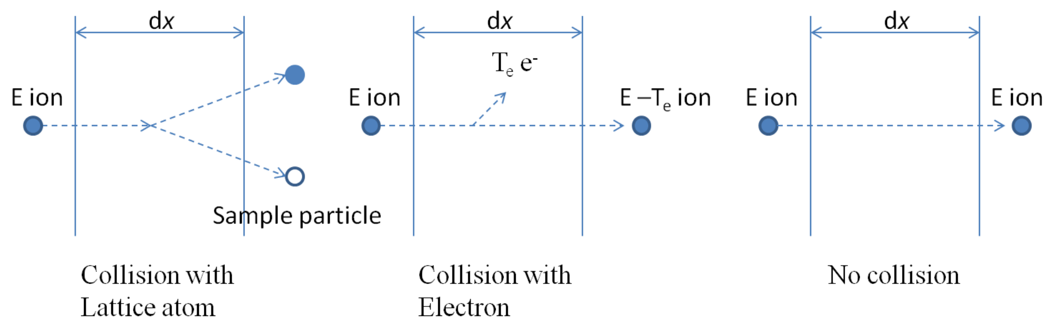

Figure 2-5 Possible processes of an ion with energy *E* on a passing through a thin layer with width, d*x*, of a solid.

Crystalline silicon can be transformed to amorphous by a sufficiently large ion fluence. The critical fluence depends on the ion, the substrate temperature, and the fluence rate, the latter parameters being particularly important for a light ion. A convenient criterion for the amorphization material in situations where essentially all of the damage is stable is that the nuclear energy deposited per unit volume should be ~ 10^{21} keV/cm^2.

The phase transition of Si crystal into amorphous will induce a decrease of the density [8]. The disordered Si atoms make the surface volume expanding at the

irradiated region.

2.2.2 Sputtering:

When energetic particles bombard a sample material, in this process, the surface atoms are removed by sequential collisions arising from the incoming particles at the near surface layers of a solid as shown in Fig 2-6. This phenomenon is called sputtering. The sputtering process determines the limit of the maximum concentration of implanted atoms that can be irradiated and remained in a target material. The yield of sputtered atoms, defined by the number of sputtered atoms per incident ion, typically lies in the range 0.5-20 and depends on the ion species, ion energy, incident angle and target material. For direct ion irradiation into a target material, the maximum concentration of irradiated species is inversely proportional to the sputtering yield. Consequently, for ion-target combinations with high sputter yields, the maximum concentration may be a few atomic percent.

Sputtering process is the erosion of a target material by energetic particle bombardment and is characterized primarily by the sputtering yield, *Y*, which is defined as:

$$Y \equiv \text{sputtering yield} = \frac{\text{mean number of emitted atoms}}{\text{incident particle}} \tag{3}$$

The sputtering process involves a complex of serial of collisions (the collision

cascade), in which various kinds of angular deflections and energy transfers are included between many atoms in the solid.

During ion irradiation, the sputtering process removes both target atoms and irradiated ions. Eventually, it reaches an equilibrium condition (steady state) is reached, where as many irradiated atoms are removed by sputtering as are replenished by irradiation. The depth distribution of irradiated atoms under this condition typically has a maximum at the surface and fall off over a distance comparable to the initial ion range.

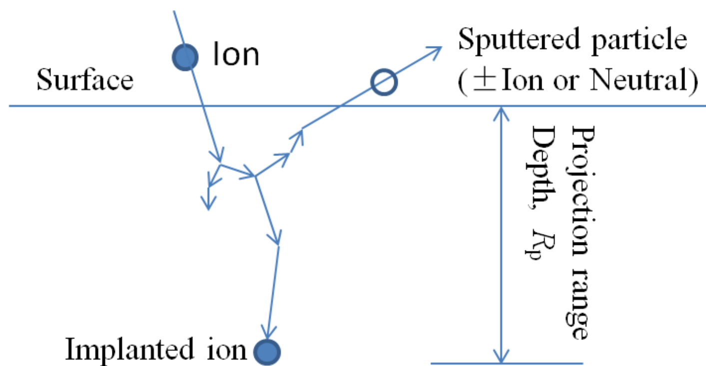

Figure 2-6 Schematic picture of sputtering and implantation process and ion solid interaction.

The steady state of surface concentrations are relatively easy to obtain. The steady state surface composition is represented as:

$$N_A / N_B = r \frac{1}{Y - 1} \tag{4}$$

N_A and N_B is the concentrations of irradiated atoms and host atoms, respectively, at the surface of the target. N_A/N_B represents the surface composition. r is the ratio of the probability for a B atoms near the surface to be sputtered to that of an A atom to be sputtered. Y is the total sputtering yield.

Since the sputtering effect remove the surface atoms, the sputtering effect can reduce the expansion height in the irradiated region. Observed swelling phenomenon should be under stood by considering the balance of the volume expansion and sputtering effect.

2.3 Annealing effect

Ion-irradiated crystals will normally contain a great amount of damages in the as-irradiated state. When we need crystal properties even after the ion irradiation the damages must be annealed. During the annealing process, irradiated ions and disorder atoms will immigrate and be incorporated into electrically active (usually substitutional) sites in the crystal lattice and residual defects are reduced to a level where carrier mobilities and lifetimes are usefully large.

Annealing is one of popular methods applied in the semiconductor field. The most popular case is recrystalization of amorphous phase Si by the annealing method. Crystalline silicon transformed into amorphous is driven by ion irradiation, can be regrown epitaxially on the underlying crystalline substrate at temperatures of about 600 ℃ in a time [41, 27]. The recrystalizing process begins at the interface between

crystal phase and amorphous phase.

Transmission electron microscopy is usually applied to study damage in ion irradiated semiconductor and its annealing behavior. This technique permits as observe study the crystalline to amorphous transition that may occur during bombardment, and to identify residual defects that are present after various annealing treatments.

3. Experimental method

3.1 Preparation of Si samples

Czochralski-grown (Cz-Si) p-type Si <100> samples, with a size of 1 $\times$ 1 cm^2 and thickness of 0.5 mm, were used in the present experiment. Before ion-beam irradiation, all of the samples were cleaned by HF acid and then soaked in ultra-pure water. The chemical treatment was performed to remove the oxidized layer on the Si crystal.

3.2 Irradiation of ion beam onto crystal silicon

Irradiation experiments were performed by using Ar^+, Kr^{2+} and C^+ ions. Those ions were irradiated into Si samples with a fluence range from 0.5×10^{16} to $8 \times 10^{16}/cm^2$. The Ar^+ and C^+ were irradiated with a fixed energy of 90 keV, and the Kr^{2+} ions were irradiated with a fixed energy 180 keV as table in 3-1.

Table 3-1.Irradiation parameters and calculated rage distribution. Projection range and longitudinal straggling of ions in silicon target are calculated by SRIM 2008.

Ion	Fluence ($10^{16}/cm^2$)	Energy (keV)	Projection range- R_p (nm)	Longitudinal straggling (nm)
Ar^{1+}	1	90	96.6	32.5
Ar^{1+}	2	90	96.6	32.5
Ar^{1+}	4	90	96.6	32.5
Ar^{1+}	6	90	96.6	32.5
Ar^{1+}	8	90	96.6	32.5
Ar^{4+}	0.15	80	86.6	29.7
Ar^{4+}	0.15	160	165.5	49.1
Ar^{4+}	0.15	320	332.3	81.2
Ar^{4+}	0.15	400	408.5	93.4
C^{1+}	0.5	90	256.6	69.71
C^{1+}	1	90	256.6	69.71
C^{1+}	2	90	256.6	69.71
C^{1+}	4	90	256.6	69.71
Kr^{2+}	1	180	104.5	27.2
Kr^{2+}	4	180	104.5	27.2
Kr^{2+}	6	180	104.5	27.2
Kr^{2+}	8	180	104.5	27.2
Kr^{2+}	4	90	57.4	16.3
Kr^{2+}	4	270	158.5	39.2

Those ion beams were prepared by a 10-GHz NANOGAN, which is an ECR ion source installed at Kochi University of Technology [42]. The ion flux was maintained $4 \times 10^{12}/cm^2\ s^{-1}$ during the irradiation. The machine consists of four parts: 1) ECR ion source, 2) acceleration system, 3) mass analyzing system and 4) irradiation system. The schematic picture of the irradiation equipment is shown in Fig. 3-1.

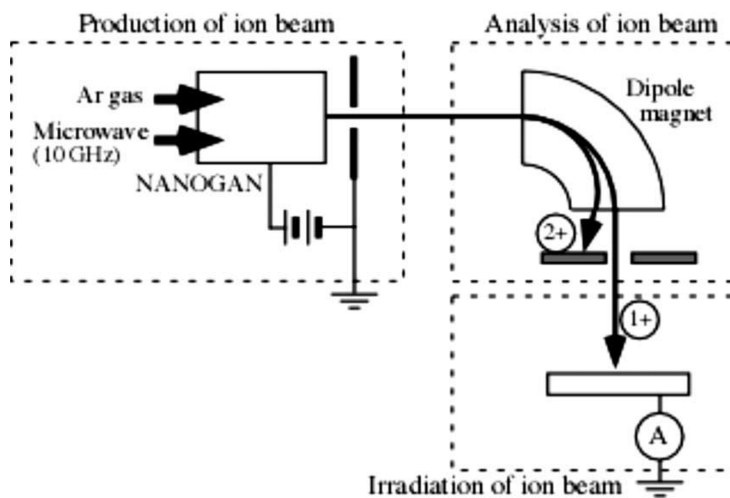

Figure 3-1. Schematic picture of the irradiation equipment of ion beam [43].

The ions, produced in the ECR ion source, were accelerated to the given for irradiation energy. In order to reduce the losses of ion beams current, all of the processes were in the vacuum condition (6.0×10^6 ~ 7.0×10^6 Pa).

The accelerated ions were irradiated in a vacuum chamber at room temperature (RT) with normal incidence through a 100 μm striped stencil mask made of stainless steel. The mask has constant four stripes, whose length and width are 2.0 mm and 0.13 mm. Owing to the masks, a portion of the irradiated areas were shielded and other

areas were exposed by the mask strips to ion beam irradiation (Fig. 3-2). It is convenient to quantify the swelling effect can be easily provide by a direct comparison of level with that of the virgin area.

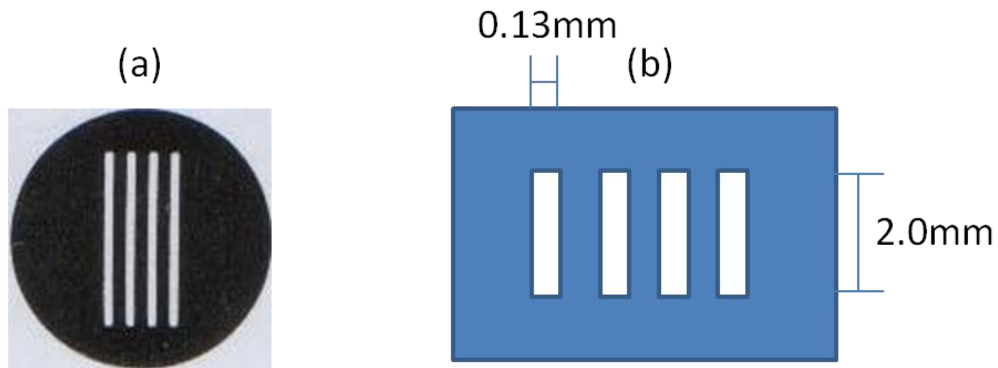

Figure 3-2. (a) Stencil mask used in ion-beam irradiation, and (b) size of stripe.

3.3 Thermal annealing

The annealing experiments were realized by desktop lamp heating unit - MILA-3000 (Fig. 3-3). The post-irradiated samples were annealed in an argon ambient environment at atmospheric pressure. The annealed temperature was in the range of 200 ～ 800 ℃ in steps of 200 ℃ and the annealing time was fixed at 60 minutes per step.

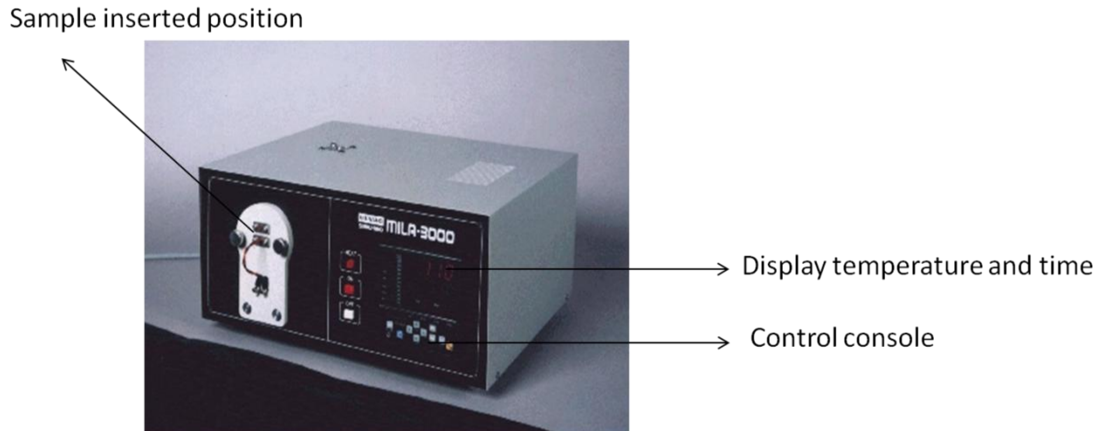

Figure 3-3. Heating equipment used to for thermal annealing.

3.4 Techniques for sample evalution

In order to measure the morphological and mechanism properties, some measurement methods were employed to evaluate the samples. The surface information was measured by using: Alpha-Step IQ Surface Profiler (Alpha-step), Atomic force microscopy (AFM) and Scaning electron microscopy (SEM). The internal information was measured by using: Raman spectroscopy (Raman) and Transmission Electron Microscope (TEM). The fundamental process of ion-beam irradiation was simulation - SRIM.

3.4.1 Alpha-Step IQ Surface Profiler (KLA-Tencor Corporation)

In this study, the alpha-step was used to measure the swelling heights of irradiated and annealed samples. The swelling height of samples was defined as the average height of irradiated region compared with level of un-irradiated region.

The Alpha-step IQ is a mechanical, stylus-based step profiler that can measure step

heights up to 2 millimeters and provide data analysis and image capture of scans. The specifications of the alpha-step are shown in table 3-2. The scanning stylus is 5-micron radius tip. The measurement parameters, applied in the present study, were: scan length 1400μm, scan speed of 20 μm/s, sampling rate of 100 Hz.

Table 3-2. Specifications of the alpha-step

Scanning stylus (standard)	5-micron radius tip, 60 angled stylus
Stylus force	15 mg (nominal setting)
Profile length (max)	10 mm in the right direction 2 mm in the left direction
Maximum step height	2 mm (for stepping down conditions only)
Scan Length	10mm
Scan Speed	2 μm/s to 200 μm/s
Sampling Rate	50, 100, 200, 500 or 1000 Hz
Vertical Range	± 10 μm (20 μm) at 0.012 Å vertical resolution ± 200μm (400 μm) at 0.24 Å vertical resolution ± 1000μm(2000μm) at 1.2 Å vertical resolution
Horizontal Resolution	0.01 μm (100 Å) at 2 μm/s scan speed
Scan Method	Moving stylus, stationary stage
Stylus Control	Manually adjustable force
Range	1.0 – 99.9 mg
Resolution	0.1 mg (~ 0.5mg standard deviation)
Optical Magnification	1) Standard: 70 – 210 x 2) High Mag. option: 160 – 480 x
Step Height Repeatability	1) At 20 μm range: 0.0008 μm (8 Å) typical standard deviation1 or 0.1% of measured vertical range. 2) At 400 μm range 0.005 μm (4000 Å) typical standard deviation or 0.2% of the measured vertical range. 3) At 2000 μm range 0.030 μm (2 μm) typical standard deviation or 0.5% of the measured vertical range.
Z control	interactive control via software
Maximum sample size	158 mm diameter

Maximum sample thickness	21mm
Maximum sample weight	1kg
Throat depth	81mm
X/Y maximum travel	151mm × 80 mm
Stage rotation	360 °, unlimited manual rotation
Leveling	manual and various software leveling of profiles

3.4.2 Atomic force microscopy

Since Binnig *et al.* [44] successfully invented the first atomic force microscopy (AFM) in 1986, AFM has been a useful tool to study the surface morphology of samples . The samples of the conductor, semiconductor and insulator etc. can be observed by the AFM. In the AFM measurement, a sharp tip attached to a cantilever is utilized to probe the sample surface as shown in Fig. 3-4. When the tip approaches the sample surface, the atoms on the sample surface exert a force (10^{-8} ～ 10^{-6} N) on the front atoms of the tip. The bending of cantilever, induced by this force, is monitored via a photo diode, which detects intensity of a reflected laser beam. The incident laser beam is directed on the top of the cantilever.

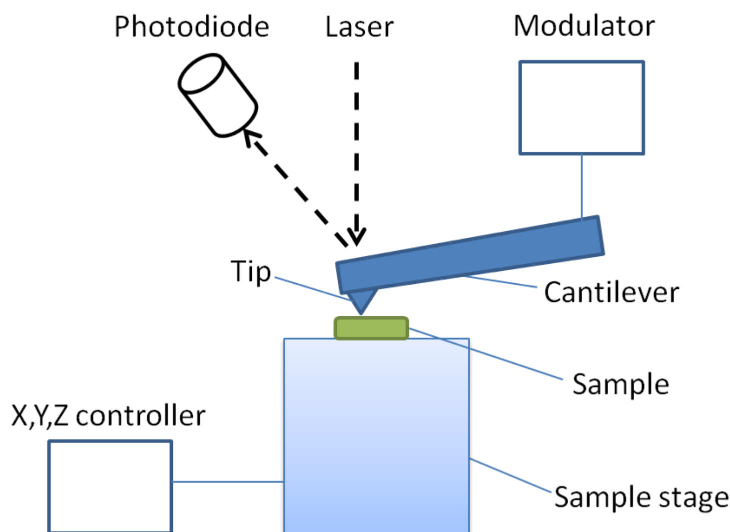

Figure 3-4. Working principle of AFM

The roughness of the sample surface is provided from AFM measurement as root mean square (R_{rms}) of the fluctuation of surface level.

$$R_{rms} = \sqrt{\frac{\sum_{n=1}^{N}(Z_n - \overline{Z})^2}{N - 1}}$$

where N is the number of the points, $\overline{Z}$ is the average height. Z_n is a height observed at a position assigned by n.

In this study, the surface morphology of annealed samples and crater depths were studied by using a Pacific Nanotechnology Nano-R™ atomic force microscope (AFM). The AFM measurement was performed by using silicon nitride tip 2-5 nm in diameter and chip tip with curvature radius of ～15nm.

3.4.3 Scanning electron microscopy measurement and mechanism

Scanning electron microscopy (SEM) is a useful method to measure the 2-dimensional surface morphology. The surface morphologies were observed by a field emission scanning electron microscope (FE-SEM) system (JEOL-JSM7400F), operating at 5 kV, was used to measure the surface of samples. SEM consists of 1) electron optical system, 2) signal receiving system, 3) power supply system and 4) vacuum system. The working principle of SEM is shown in Fig. 3-5.

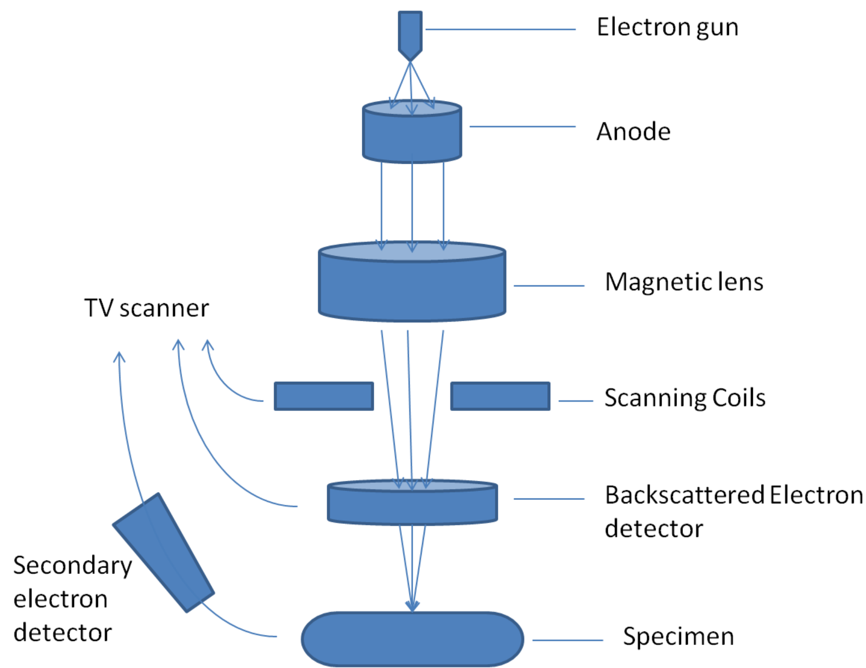

Figure 3-5. Working principle of SEM

3.4.4 Raman spectroscopy

The scattering occurs when a beam of monochromatic light passes through a crystal a crystal, and the scattering involves Rayleigh and Raman scattering (Fig. 3-6). The monochromatic laser light with frequency υ_0 excites the sample. 1) The molecule absorbs a photon with υ_0, the excited molecule returns back to the ground state and with emitting emits light with same frequency υ_0 for excitation. It is named Rayleigh scattering. The Rayleigh scattering is caused by the elastic collision between the incident photons and the phonons in materials, thus generates light with the same vibrations frequency as the incident ray. 2) The molecule absorbs a photon υ_0, part of the photon energy is transferred to Raman-active mode with frequency υ_1. The final frequency of the scattered light is $\upsilon_0 - \upsilon_1$. It is named Stokes Raman scattering. The

Raman scattering is induced by the inelastic collision between incident photons and phonons in the materials, hence produce the incident photons with different vibration frequency [45]. 3) The molecule absorbs a photon υ_0, part of the photon energy is transferred to Raman-active mode with frequency υ_1. The final frequency of the scattered light is $\upsilon_0 + \upsilon_1$. It is named Anti - Stokes Raman scattering. The intensity of Rayleigh scattering is about 10^{-3} of the incident light and the Raman scattering is about the 10^{-3} of the Rayleigh scattering. Raman scattering is typically very weak, and as a result the main difficulty of Raman spectroscopy is separating the weak inelastically scattered light from the intense Rayleigh scattered laser light.

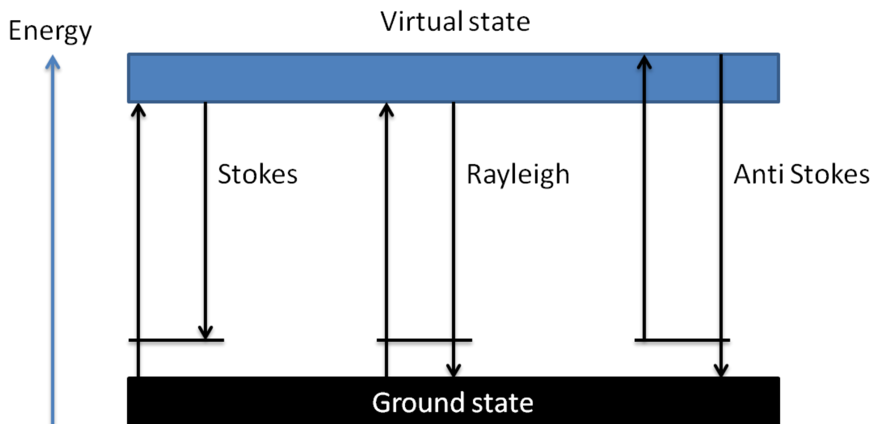

Figure 3-6. Energy level diagram showing the states involved in Raman signal. The line thickness is roughly proportional to the signal strength from the different transitions.

The Raman shift is strongly influenced by microscopic structure, impurity and residual strains, which lead to changes in phonon frequencies - shift of peaks, broadening of Raman peaks, and breakdown of Raman selection rules. Laser Raman

spectroscopy can detect the amorphous silicon as well as residual stress in silicon wafer.

There are a number of advanced types of Raman spectroscopy, such as surface-enhanced Raman, resonance Raman, tip-enhanced Raman, polarised Raman, stimulated Raman (analogous to stimulated emission), transmission Raman, spatially offset Raman, and hyper Raman.

In this study, Raman spectroscopy was applied to characterize defects, physical and chemical interactions of the irradiated ions in silicon. Raman spectra were measured at room temperature under the backscattering geometry using the 532 nm of laser (HR 800 Horiba). The measurements were performed under same condition for each measurement.

3.4.5 Transmission Electron Microscope (TEM)

The transmission electron microscope (TEM) operates on the same basic principles as the optical microscope, except for the uses of electrons instead of light. What you can see with a light microscope is limited by the wavelength of light. TEMs use electrons as "light source" and their much shorter wavelength makes. It possible to achieve much better get a resolution a thousand times better than with a optical microscope. The basic working principle is shown in Fig. 3-7.

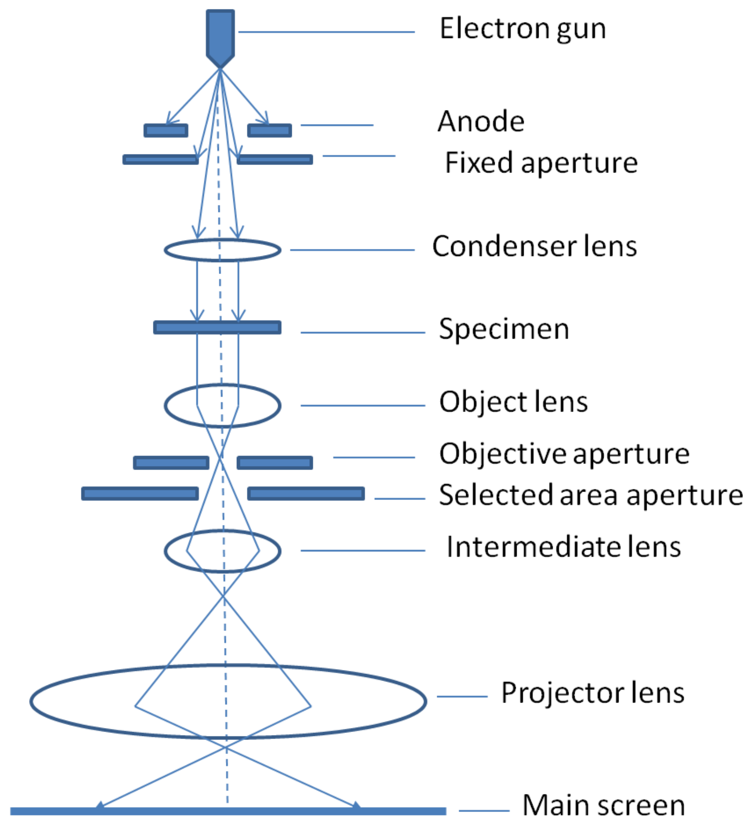

Figure 3-7. Working principle of TEM

An electron gun at the top of the microscope emits the electrons that travel through vacuum in the column of the microscope. Instead of glass lenses focusing the light in the light microscope, the TEM uses electromagnetic lenses to focus the electrons into a very thin beam. The electron beam then travels through the specimen to be evaluated. Depending on the density of the material present, some of the electrons are scattered and disappear from the beam. At the bottom of the microscope, the unscattered electrons hit a fluorescent screen, which gives rise to an image of the specimen with its different parts displayed in varied darkness according to their density. The image can be observed directly by the operator or photographed with a camera.

In TEM, an acceleration energy of several hundred keV is utilized to illuminate the samples, which thickness is typically ～100 nm. There are two fundamental imaging models TEM: diffraction and image model.

In the diffraction mode, normally the objective aperture is opened wide and the selected-area aperture is inserted to select the area of interest, here comes the term selected-area electron diffraction (SAED). In the image mode, the selected area diffraction (SAD) aperture is usually opened wide and the objective aperture is inserted to select interested spots.

Bright field (BF) and dark field (DF) regimes are usually utilized to take photos of samples. In the BF regime, the objective aperture is adjusted so that it does not intercept the transmitted spot. Several diffracted spots around the transmitted spot can be selected also. However, it is a trade-off between the brightness and contrast, the more selected spots make the image brighter, and male the image worse contrast. To take a simple DF images, the objective aperture is adjusted so that it intercepts the transmitted spot. As a result, merely diffracted spots are selected. DF images taken in this way are generally not preferable because the diffracted beams travel off from the optic axis, which increases aberration and astigmatism.

High-resolution transmission electron microscopy (HRTEM) is an imaging mode of the transmission electron microscope (TEM) that allows the imaging of the crystallographic structure of a sample at an atomic scale. HRTEM images result from phase-contrast. When electron waves travel across very thin sample (typically less than 50 nm), as the result of scattering by the sample's atoms, the electron

waves which pass through the sample, do not change with uniform amplitude, but obtain phase shift.

In this study, the microstructural evolutions of the Ar-irradiated Si target was studied by cross-sectional transmission electron microscopy (TEM) using a JEOL 2100F operating at an accelerating voltage of 200 kV. Structural changes associated with ion irradiation were observed by bright-field images (BFIs) and HRTEM. The samples were prepared by focus ion beam (FIB) - FEI QUANTA 3D 200i operating at an accelerating voltage of 30 kV and the ion species is Ga. Pt atoms were deposited on the sample surface to form a protection layer. The Si sample was cut into a small piece of sample, and was placed on a copper holder with three convex protrusions. Finally, prepared piece was milled to thickness of ～100 nm by mean of the focused Ga ion beam.

3.4.6 Simulation of irradiation effect by means of SRIM

The simulation of ion beam irradiation process has been developed several decades. The stopping and Range of Ions in Matter (SRIM), developed by James F. Ziegler, Jochen P. Biersack, and Matthias D. Ziegler since 1980s, is a popular software to calculate the irradiation effect [46]. The software has been SRIM is based on a Monte Carlo simulation method, namely the binary collision approximation with a random selection of the impact parameter of the next colliding ion TRIM is a core component contained in programs of SRIM. SRIM can calculate the stopping and

range of ions with energy of 10 eV – 2 GeV/amu into matter using a quantum mechanical treatment of ion-atom collisions. During the collisions, the ion and atoms have a screened Coulomb collision, including exchange and correlation interaction between the overlapping electron shells.

There are advantages of SRIM software: The three-dimensional distribution of the ions in the solid and its parameters, such as penetration depth, its spread along the ion beam (called straggle) and perpendicular to it, all target atom cascades in the target are followed in detail. We can get the value of concentration of vacancies, sputtering rate, ionization, and phonon production in the target material. The disadvantages of SRIM software: It doesn't take account of the crystal structure dynamic composition changes by different irradiation parameters. It can not simulate the various irradiation temperatures.

Chapter 4. Control of Swelling Height of Si Crystal by Irradiating Ar Beam

4.1 Definition of the swelling height

Fig 4-1(a) shows an image around a border between the irradiated and un-irradiated area measured by AFM. A swelling structure can be seen clearly at irradiated area in the figure. Fig 4-1(b) shows a cross-sectional profile of the swelling structures, measured by Alpha-step. In this figure, the top part and bottom part correspond to the irradiated part and the un-irradiated part, respectively. These figures indicate that the swelling structure, formed by Ar beam irradiation, is regular enough to define the swelling height. The swelling height is defined to be the distance between the averaged levels of irradiated and un-irradiated part for each stripes. As shown in the following section, the observed swelling height depends on the irradiation parameters of Ar beam. The advantages of this nano-structure are (1) the regular border in this area, (2) a good reproducibility and (3)integration of nano-structure and substrate.

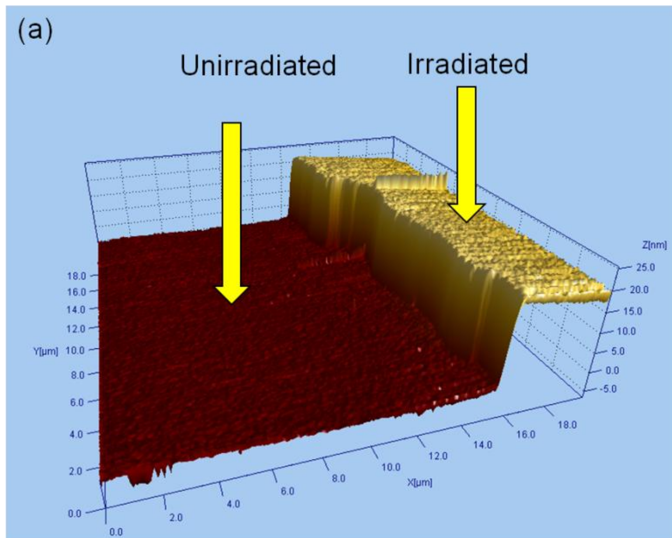

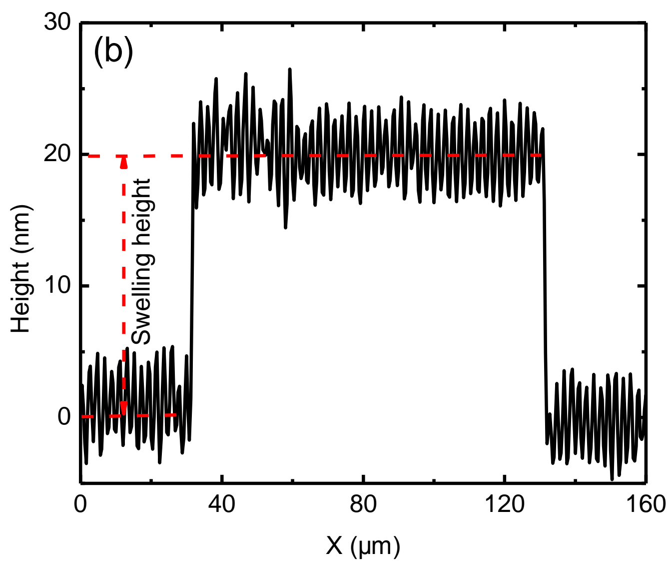

Figure 4-1. Swelling structure, fabricated on Si crystal, observed by (a) AFM and (b) Alpha-step. The structure was fabricated by irradiating Ar^{1+} beam on Si with an energy of 90 keV and a fluence of 10^{16} /cm^2.

4.2 The fluence dependence

Fig 4-2 shows the swelling height as a function of the fluence of Ar^{1+} beam with the energy of 90 keV. As the fluence increased, the swelling height increased up to about 60 nm. The error bars in the figure show the standard deviation of the observed

height of swelling structure. At the fluence of 10^{16}/cm^2, which is larger than the threshold fluence to produce the amorphous layer [47, 48], the swelling height of 15nm was observed. The number of disorder atom in Si crystal increases continuously with the irradiated fluence [49]. Therefore, it is evaluated that observed continuous increasing in swelling height would be explained by the cumulative result of amorphous defect.

Fig 4-3 shows the swelling height as a function of the fluence of Ar^{4+} beam with the energy of 240 keV at fluence range from 3×10^{14} to 1.56×10^{16} /cm^2. The swelling height increased with the fluence as observed with Ar^{1+} beam. At the fluence of 3×10^{14} /cm^2, the swelling height of 3 nm was observed. The continuous increasing of swelling height is similar with that for Ar^{1+} beam shown in Fig 1. According to ref. [50], highly charged ion (HCI) beam can deposit higher energy in the irradiated material and induces unique phenomena. Therefore, it is probable that HCI beam would have the widely applications for irradiation and producing swelling structures.

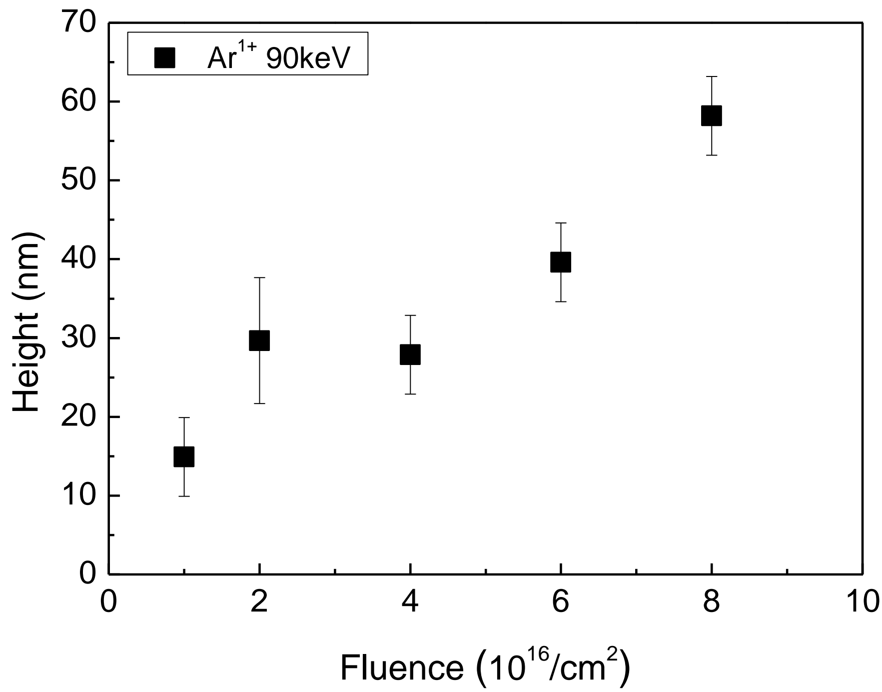

Figure 4-2. Swelling height as a function of the fluence of Ar^{1+} ion with 90keV.

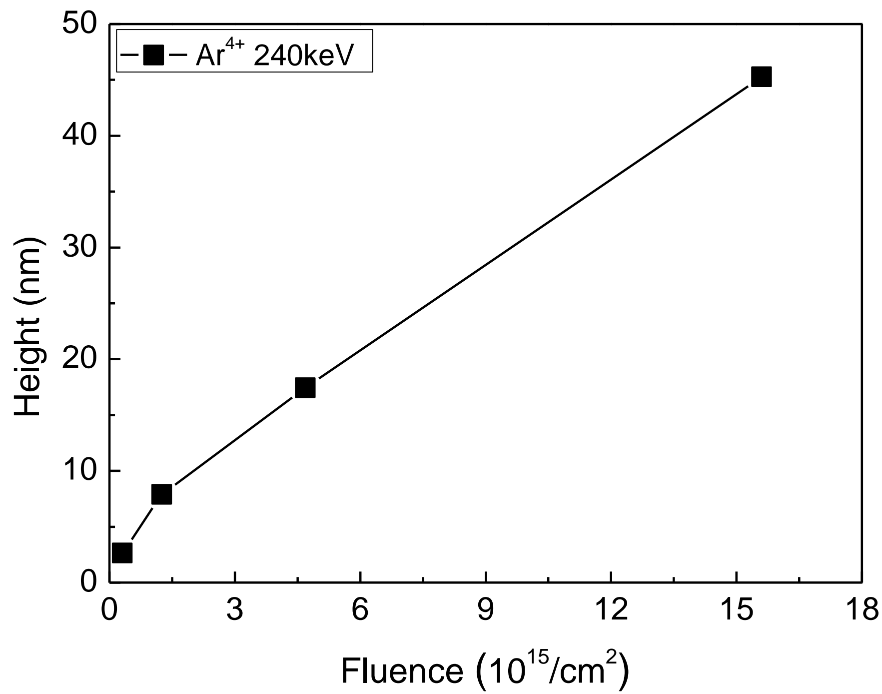

Figure 4-3. Swelling height as a function of the fluence of Ar^{4+} ion with 240 keV.

4.3 The energy dependence

Fig 4-4. shows the swelling height as a function of the energy of Ar^{4+} beam with the fluence of 1.5×10^{15} /cm^2. The swelling height increases with the irradiation energy increasing. At the energy of 80 keV, the swelling height of 5 nm was observed. As the beam energy increases, projection range of irradiation increase [51, 5]. As shown in Fig 4, the swelling height indicates clear relation with the irradiation energy of Ar beam. This result indicates the irradiation of energies performed an obvious influence to swelling height. Therefore, the energy of irradiated ion is another important parameter in fabricating the swelling structure.

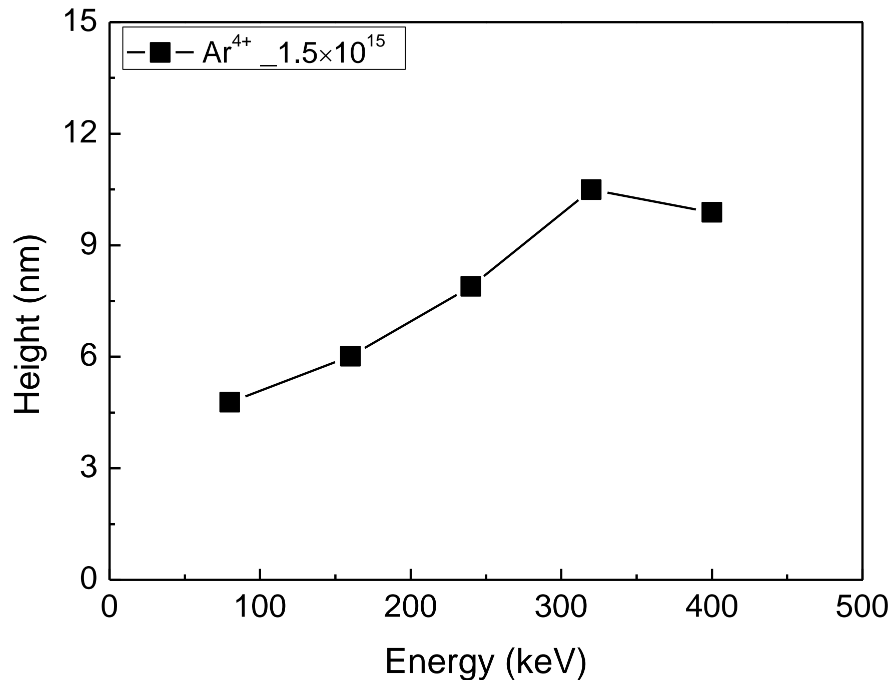

Figure 4-4. Ion energy dependence of swelling height.

4.4. Comparison with the simulation

It is evaluated that the swelling height would be explained by two contributions: additional volume induced by implanted ions and defect production. As the contribution of irradiation effect of Ar atoms is estimated to be about few% of observed swelling height, the defect production would be dominant in the swelling phenomena.

As shown in Fig 4-5, the swelling height could be controlled by beam energy. In order to understand the relation between energy and swelling height based on the defect production, the SRIM 2008 [46] was applied to simulate the ion irradiation process.

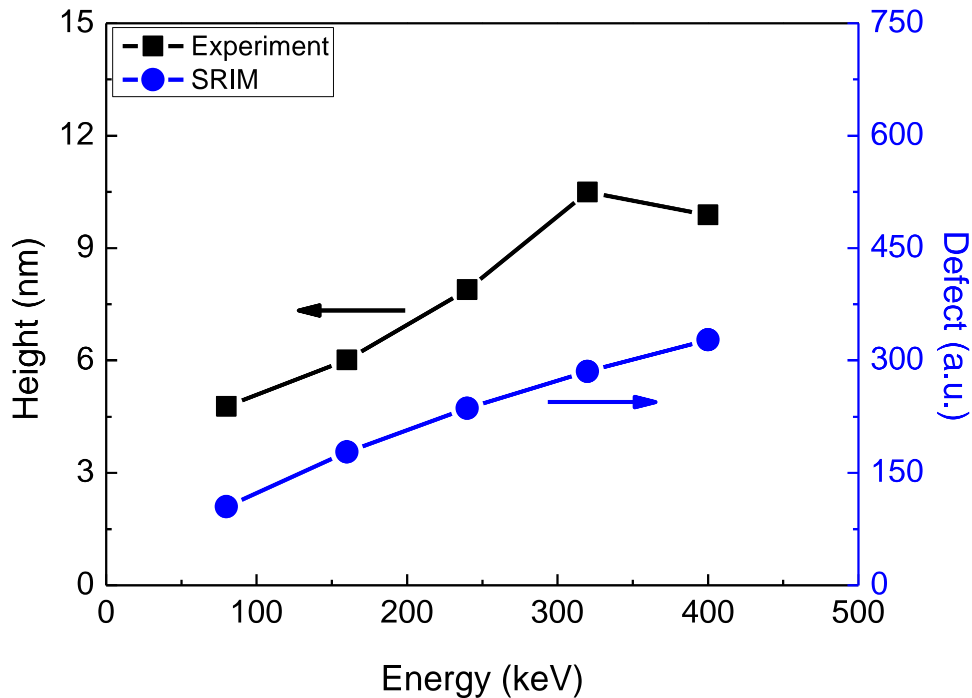

Figure 4-5. Energy dependence of observed swelling height and amount of defect induced by ion beam in Si crystal calculated by SRIM.

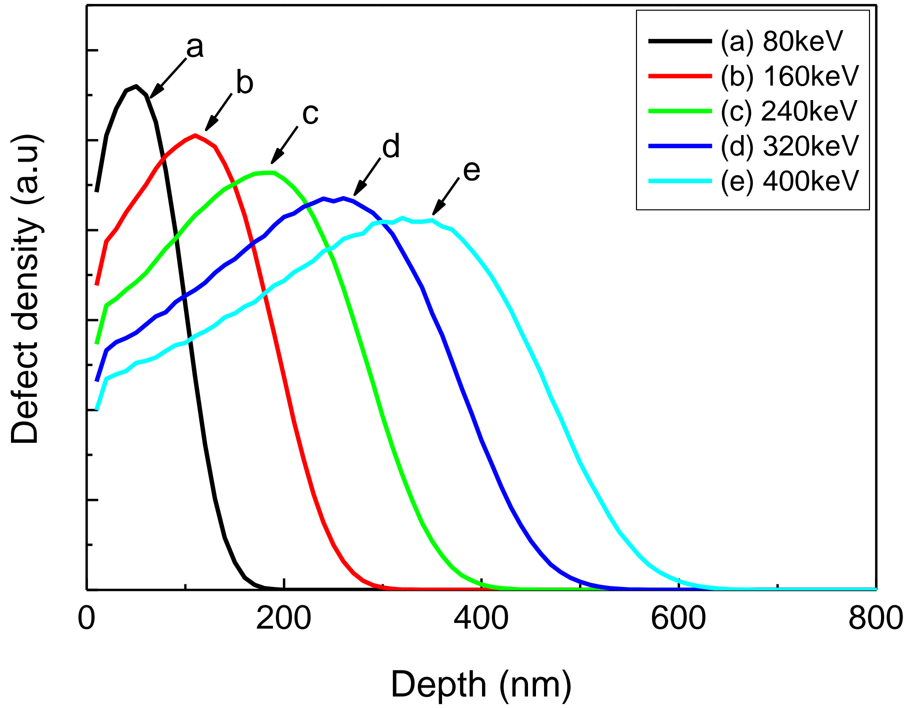

Figure 4-6. Energy dependence of depth profile of ion-beam induced defect in Si crystal calculated by SRIM.

Fig 4-6. shows the depth distribution of defects in Si crystal produced by Ar beam with various beam energies, which is calculated by SRIM 2008. It can be seen clearly that the distribution expands with the beam energy proportionally. On the other hand, the maximum defect density decreases gradually. The amorphization of Si crystal is caused by the ion-beam induced defects [52-54]. The formation of amorphous layer would lead to the volume expansion and result in swelling height of Si surface. According to this simple model, the relation between the swelling height and the amount of defect can be represented as：

$$H \propto N_{\mathbf{D}} \qquad \mathbf{(1)}$$

Where H is the swelling height and N_D is the amount of defect in Si crystal.

The amount of ion-beam induced defect can be calculated by integrating the depth distribution as shown in Fig. 4-6. In Table 4-1, the characteristics of defect calculated by SRIM and observed swelling height are summarized for various energies. From this table, the amount of defect increased with increasing irradiated energy in simulated results. This calculated result is consistent with experimental data that the observed swelling height increases with increasing irradiated energy in experimental data as shown in Fig 4-5. As a result, a simple method, which is introduced in this section, is a useful to understand swelling height by using the defect density calculated by SRIM.

Table 4-1. Energy dependence of defect distribution in Si calculated by SRIM

Ion energy (keV)	Ion charge	Depth at maximum defect density (nm)	Maximum defect density (arbitrary unit)	Amount of defect (arbitrary unit)	Observed swelling height (nm)
80	4+	50	1.12	104.76	4.78
160	4+	110	1.01	178.08	6.01
240	4+	190	0.927	236.40	7.89
320	4+	260	0.871	285.33	10.49
400	4+	320	0.827	327.50	9.88

As mentioned above, the swelling height can be considered as a result of expansion of Si crystal. The expansion is induced by defect in Si crystal. The expansion phenomena is evaluated by using degree of expansion defined as：

$$\textbf{Degree of expansion} \equiv \frac{H}{D}, \quad \textbf{(2)}$$

Where H is the swelling height and D is the depth, which characterizes defect distribution.

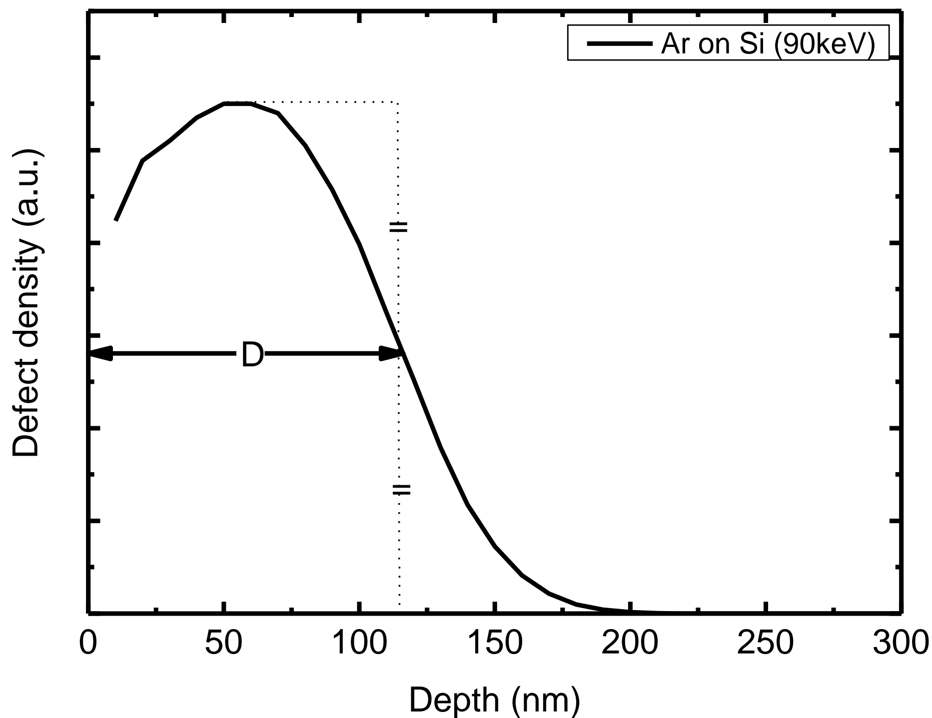

Figure 4-7. Density distribution of defect calculated by SRIM.

Fig. 4-7 indicates a density distribution of defect calculated by SRIM, and D is

defined by the depth at which the density becomes a half of its maximum. Degree of expansion, which is provided from observed *H* and *D* evaluated as mentioned above, is tabulated in Table 4-2 with the previous results with Si beam. In spite of similar irradiation conditions, degree of expansion of Ar-irradiated Si crystal is about two times larger than that of Si-irradiated Si crystal. The result indicates an enhancement of irradiation effect for heavier ions, and are consistent with previous experimental results [55]. For further discussion, more experimental studies are required.

Table 4-2. Degree of expansion of Si crystal irradiated by Ar and Si ions at room temperature

	Fluence ($\times 10^{16}/cm^2$)	E (keV)	H (nm)	D (nm)	Degree of expansion (H/D)
Ar^+ on Si	6	90	39.6	115	0.344
Si^+ on Si	6	80	22[11]	145	0.152
Ar^+ on Si	4	90	27.87	115	0.242
Si^+ on Si	3.6	80	17[11]	145	0.117

The reason of these phenomena are the irradiated ion enlarged kinetic energy, then irradiate ions can induce larger number of defect atoms. According to the above discussion, we can conclude that the swelling height depends on the amount of irradiation-induced defects.

4.5 Stability of swelling structure at room temperature

Fig 4-8. shows the swelling height of the Si samples irradiated by Ar^{1+} beam with the fluence of 1×10^{16} and 2×10^{16} /cm^2 as a function of elapsing time keeping atmosphere at room temperature. During this period of time, the observed swelling height does not change with in precision of measurement. Therefore, it is concluded that the swelling height is stable at least for two months in atmosphere at room temperature. The stability of swelling structure produced by ion beam irradiation indicates that the irradiation defect is stable at room temperature. This method producing the stable swelling structure has the wide application in various fields.

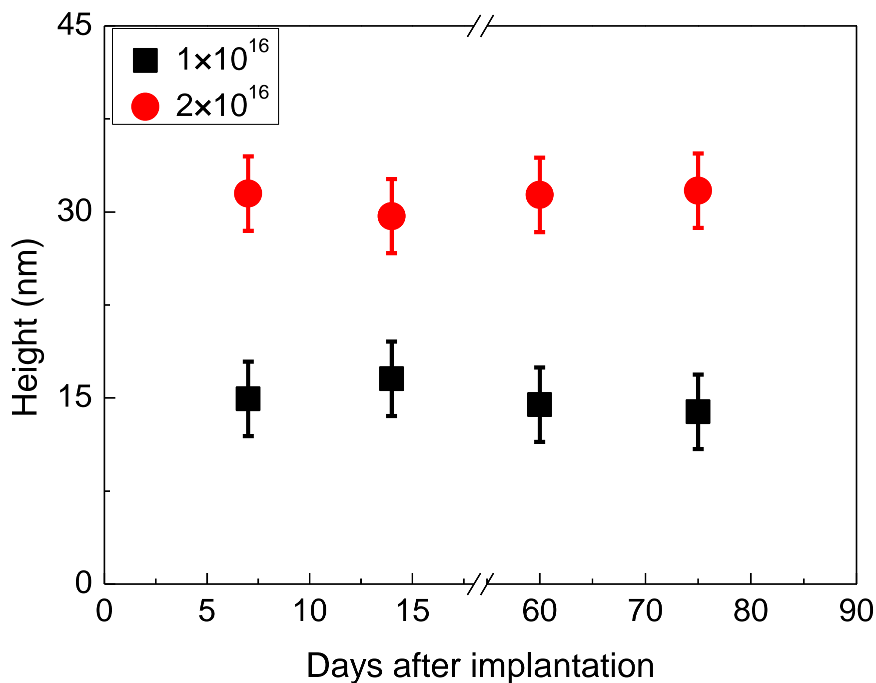

Figure 8. Swelling height of Si crystal as a function of time after the irradiation.

Chapter 5. Swelling and annealing phenomena of Si crystal irradiated by Ar and C ion beams

5.1 Comparison of Si swelling height produced by Ar and C beams

For both ions, the expansion effect is observed at the irradiated area in experiment. Fig. 5-1 shows the swelling height as a function of the fluence of Ar^+ and C^+ beams with energy of 90 keV, which is larger than the threshold energies for damage effect. The error bars in the figure show the standard deviation of the observed height of the swelling structure.

In case of the Ar^+ irradiated swelling height, the range of irradiated fluence was $10^{16}/cm^2 \sim 8 \times 10^{16}/cm^2$ and the swelling height increased up to about 60 nm. Since additional volume induced implantation of Ar atoms is evaluated to be a few percentage of observed height.it was observed that the swelling height has a strong relation with irradiated damage. The numbers of disorder atoms increases with the irradiation fluence [56]. In case of the C^+ irradiated swelling height, the range of fluence was $5 \times 10^{15}/cm^2 \sim 4 \times 10^{16}/cm^2$ and the swelling height inceases up to a few nanometer about 5 nm. C beam irradiation induces not only amorphous Si, but also $Si_{1-x}C_x$ amorphous alloy states. The transformation of crystal Si into Si-C compounds does not induce a remarkable change in the Si atomic density, but requires mainly the addition of a sufficient number of C atoms to the lattice and some atomic rearrangement, besides the emission of a few silicon self-interstitials Si_I [57]. Therefore the swelling height mainly comes from amorphous Si induced by

C beam irradiation. These two results are consistently understood with the nuclear stopping power contribution calculated by SRIM. In the same irradiation parameter (energy fluence), the Ar beam irradiation produced higher swelling height compared with the C beam irradiation.

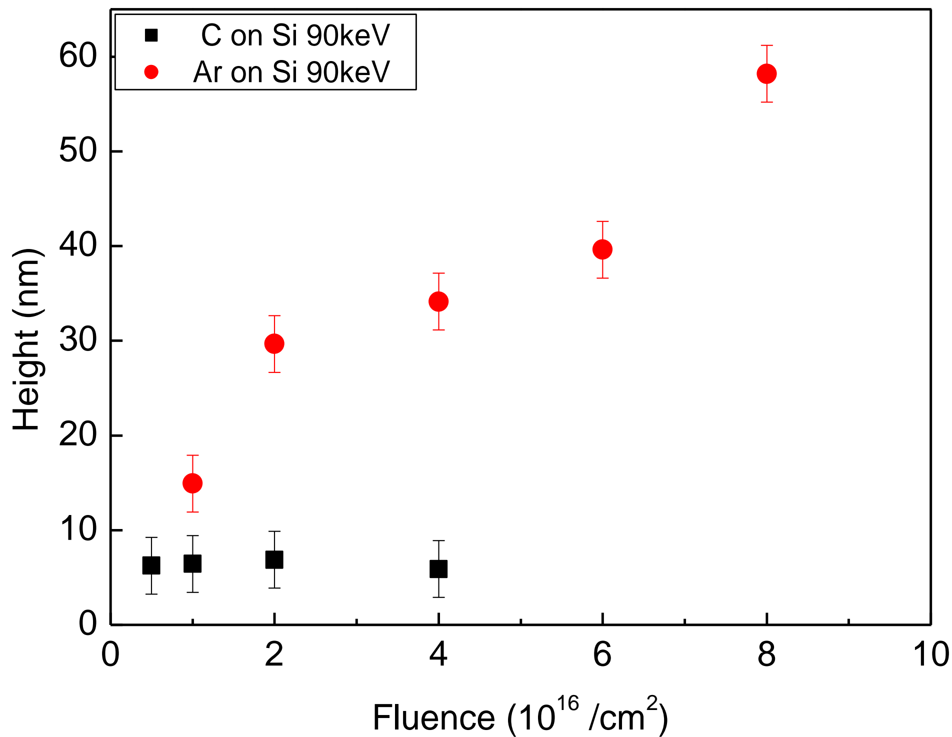

Figure 5-1. Swelling height as a function of the fluence of Ar^{1+} and C^{1+} ions.

5.2 Simulation of

SRIM 2008 was used to perform full cascade simulations for both ion irradiations [46]. The density of Si target 2.321 g/cm^3 and the threshold displacement energy 15 eV were used in the calculation. We calculated the projection range of ions at 90 keV and the dpa (displacement per atom) distribution at a depth corresponding to the ion fluencies, and the results are show in Fig. 5-2. The depth distribution of the Ar

and C ions is inhomogeneous. The projection ranges of Ar and C beams in Si crystal were 99.1 nm and 256.6 nm, respectively. The dpa values increase with increasing the fluence of both ions. In the case of a uniform fluence, the Ar beam could produce a larger number of displaced Si atoms compared with the C beam. This results means that the same irradiation parameters, Ar beam can induce larger number of damages than the C beam. SRIM calculation also provides stopping power as shown in Table. 5-1. In case of Ar ions, the Ar nuclear stopping power is larger than electronic stopping power. However, in case of the C beam, nuclear stopping power is smaller (~ 1/6) than electronic stopping power. This result means that most of the C ion energy is lost through electron collision process. As a result, SRIM calculation shows different energy deposit process for Ar and C ions in Si target. The difference causes the Ar beam can produce larger damage than the C beam in the Si target under the same irradiation condition.

(a)

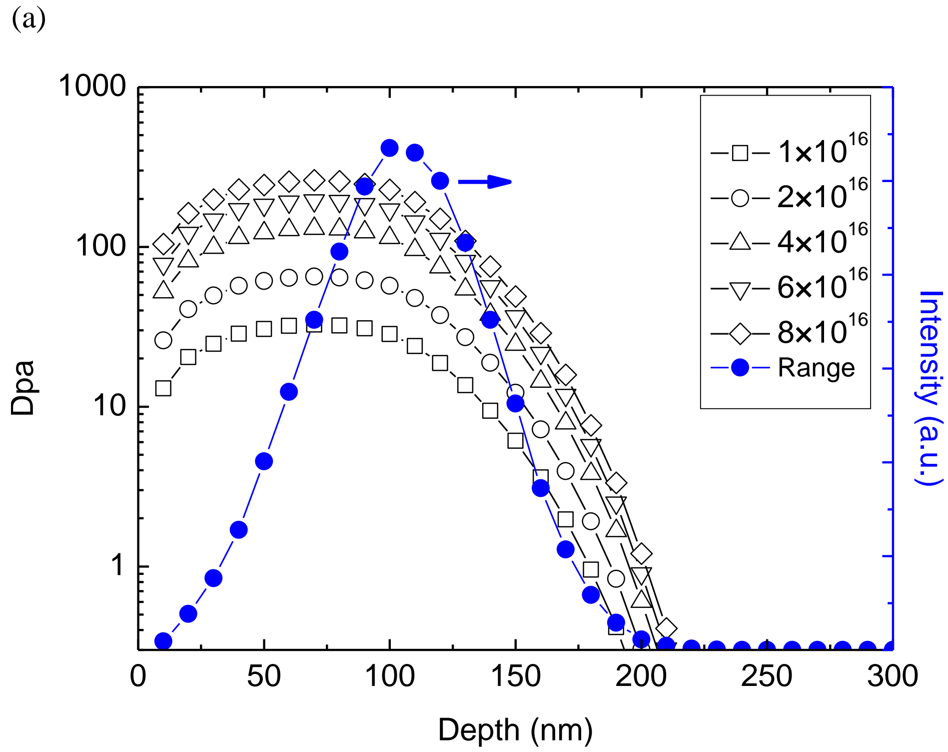

(b)

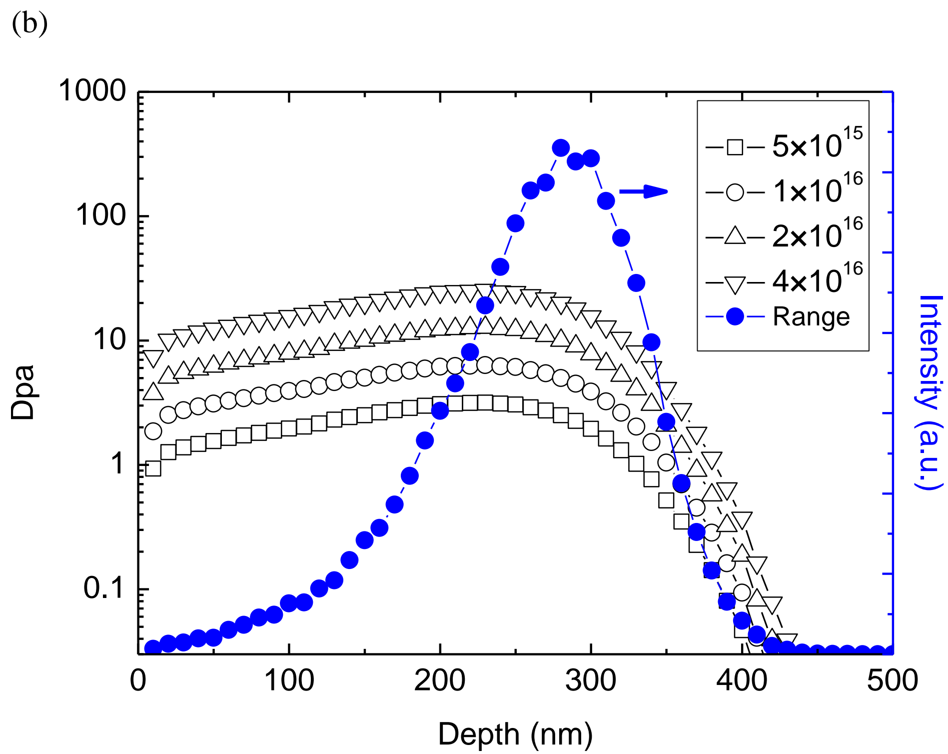

Figure 5-2. (a) Depth distribution of Dpa induced by Ar^{1+} ions and range. (b) Depth distribution of Dpa induced by C^{1+} ion and range.

Table 5-1. Projection range (R_p), mean electronic stopping power $(-dE/dX)_e$, mean nuclear stopping power $(-dE/dX)_n$ of ions in Si. The average number of displaced atoms per ion and per path length unit (dN_d/dx), calculated by SRIM2008.

Ion	Energy (keV)	R_p (nm)	$(-dE/dX)_e$ (keV/nm)	$(-dE/dX)_n$ (keV/nm)	dN_d/dx (/ion/nm)
Ar^+	90	99.12	0.3479	0.4911	1.78
C^+	90	256.6	0.2869	0.0451	2.97

5.3 Modification induced by thermal annealing

The images of Si crystal surface, which was processed by each thermal annealing, are shown in Fig. 5-3. Four strip traces in the figures indicate the irradiated region. The annealing temperature was from 200 to 800 ℃ in steps of 200 ℃. In the case of Ar^+ beam irradiation, the irradiated pattern remains up to 800 ℃, as shown in Fig. 5-3(a). In contrast, in the case of C beam irradiation, the irradiated pattern start disappearing at 600 ℃, and completely disappears at 800 ℃, as shown in Fig. 5-3(b). The Ar and C irradiated Si samples present different annealed appearances.

(a)

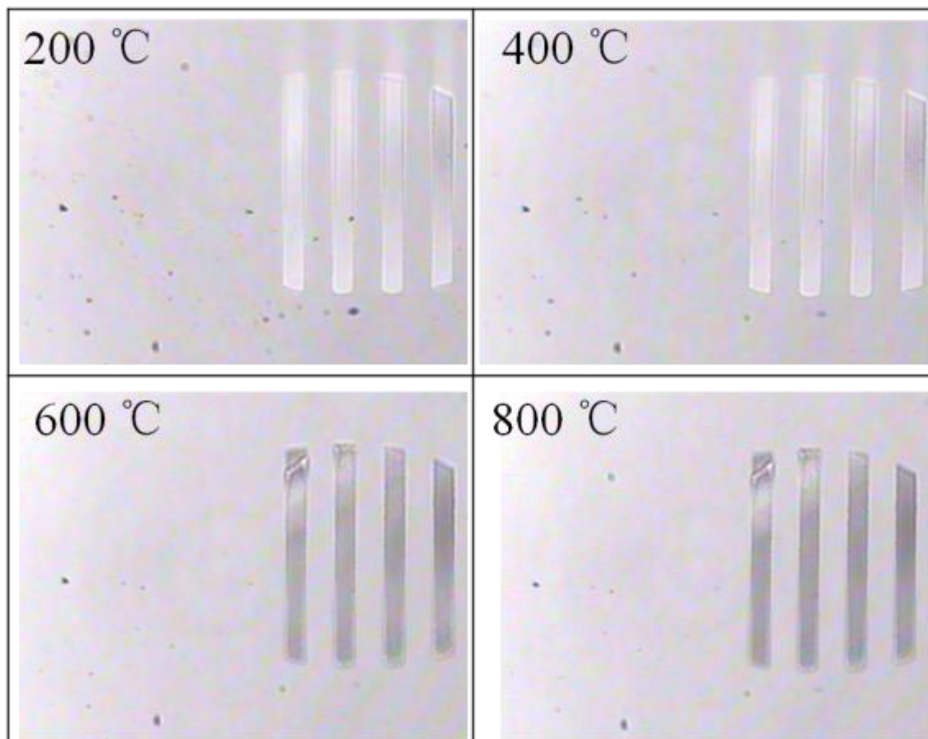

(b)

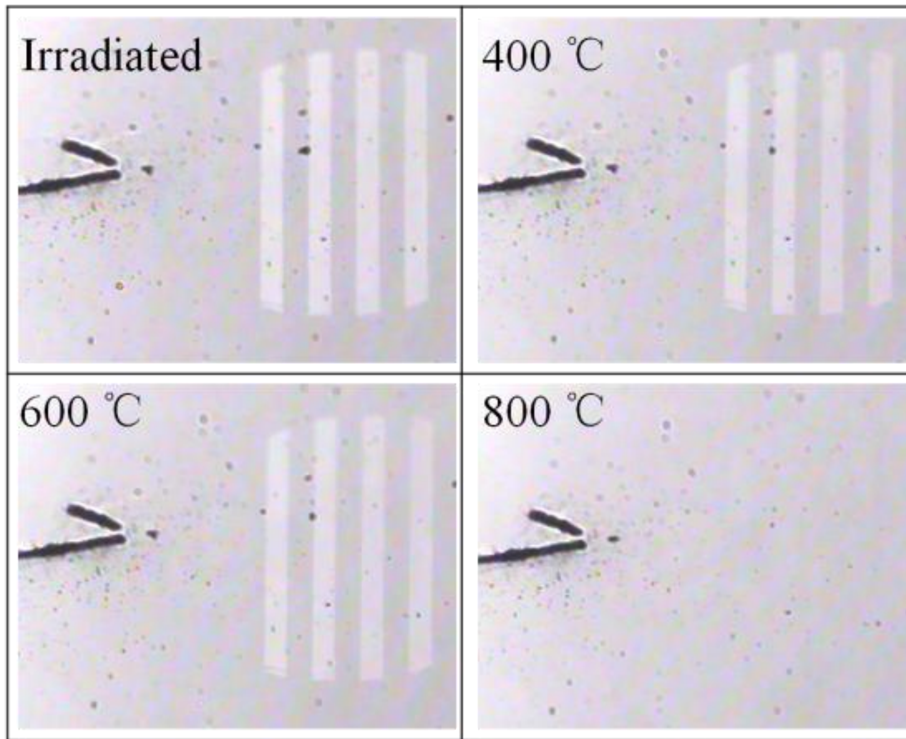

Figure 5-3. Images of Si surface pattern irradiated by (a) Ar^{1+} irradiated Si. (b) C^{1+} irradiated Si.

Fig. 5-4 shows modification of swelling height of Si samples irradiated (Ar^{1+} and C^{1+} irradiated Si, $4\times10^{16}/cm^2$ and 90keV) as a function of annealing temperature. For the samples, the characteristics for the swelling height were observed with step-by-step annealing at various temperatures. The swelling height shows no significant modification until being annealed up to 400 ℃ for both samples. In case of Ar beam irradiation, the swelling height shows suddenly increase at a temperature of 600 ℃ and continuous increased up to 800 ℃. On other hand, In the C irradiated sample, the swelling height shows decreasing at 600 ℃, and the swelling height was almost close to the contributed swelling height of irradiated C ions volume at 800 ℃.

The residual height of C^+ irradiated Si sample, which was annealed sample at 800 ℃ could be related to the amorphous $Si_{1-x}C_x$ alloy [58].

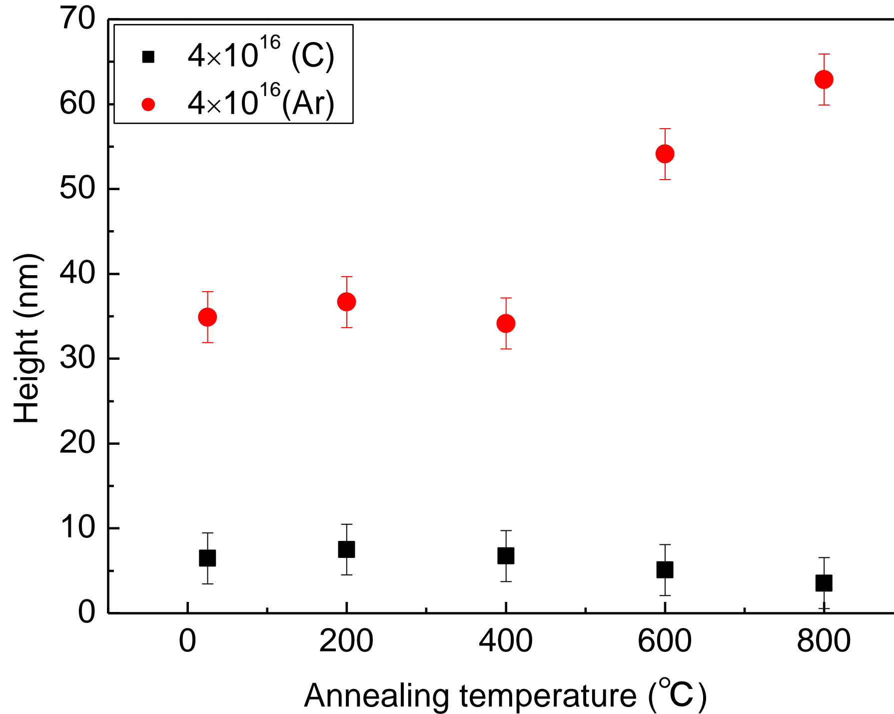

Figure 5-4. Swelling height of annealed Ar and C irradiated Si samples as a function of various temperatures.

The C^+ beam irradiated Si sample had the different annealing characteristics and mechanisms from the Ar beam irradiated one. The swelling height does not show any evident measureable change until 400 ℃. Nevertheless, a significant reductive tendency of the swelling height was observed annealed at 600 ℃, and continued to reduce further when annealed at 800 ℃. In the C beam irradiated Si target, there are c-Si, amorphous Si and $Si_{1-x}C_x$ amorphous alloy states [59]. By means of the annealing process, amorphous Si, induced by ion beam irradiation, is recovered [60, 61], and the implanted C atoms are diffused in silicon at 800 ℃, as observed by

Werner *et al.* [62]. The swelling height decreased can be explained by recovering a recrystallisation process. During the annealing process, the amorphous layer transforms into an $Si_{1-x}C_x$ amorphous alloy mixed with a small quality of SiC [58, 57]. The transformation of amorphous Si into crystal Si and $Si_{1-x}C_x$ alloy induces the change of a decrease in the volume, so the swelling height decreases upon being annealed at high temperature.

Chapter 6. Experimental study on the mechanism of Si swelling phenomenon by Kr beam

6.1 Swelling effects induce by Kr beam irradiation

Fig. 6-1 shows the swelling height of Si crystal irradiated by Kr^{2+} beam of 180 keV as function of fluence. The error bars in the figure show the standard deviation of the observed height of the swelling structure. Concerning the Kr^{2+} irradiated swelling height, the fluence range was $0.5 \times 10^{15}/cm^2 \sim 8 \times 10^{16}/cm^2$ and the swelling height increased with the irradiation fluence up to about 10 nm. The measured swelling height mainly comes from irradiated defect and irradiated Kr atoms in Si target.

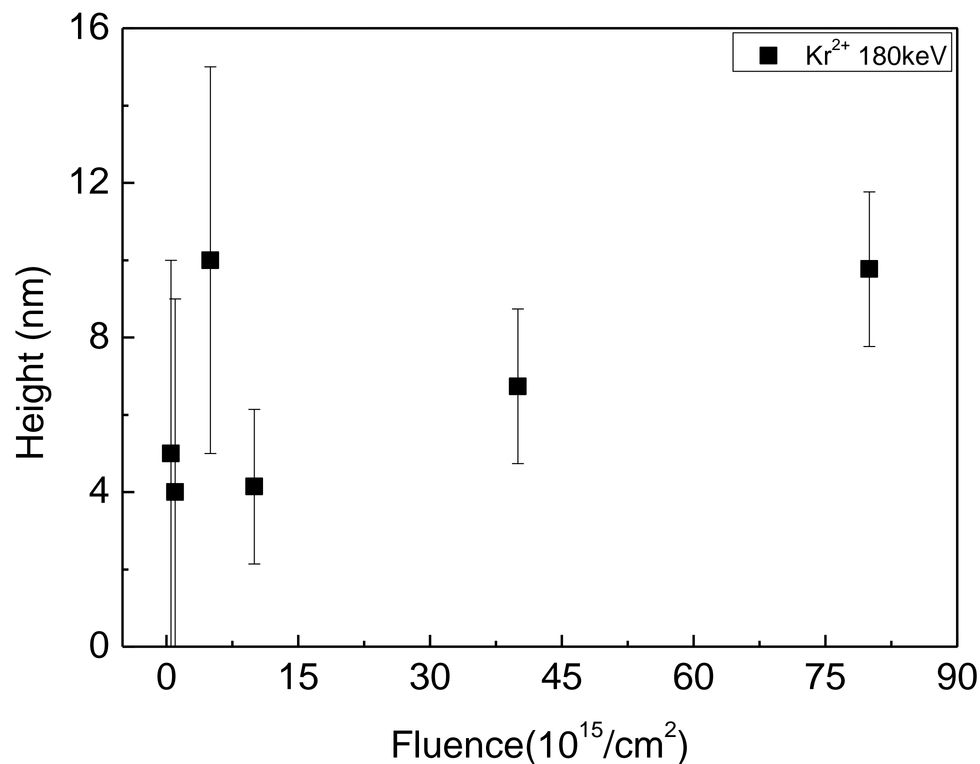

Figure 6-1. Swelling heights as a function of the fluence of by Kr^{2+} ions.

SRIM 2008 calculations were performed for Kr ion irradiation (full cascade simulations) [46]. The Si target of density 2.321 g/cm^3 and the threshold displacement energy of 15 eV were used in the calculation. We calculated the range of ions and electronic and nuclear energy losses of ions in the Si sample irradiated by 180 keV. These results were distributed at a depth about 200 nm, which is shown in Fig. 6-2. In the irradiation condition, nuclear energy loss is about 4 times larger than electronic energy loss at the beginning of the ion range. This is easy to produce the amorphous layer, which shows the Kr beam can produce huge damage in the irradiation layer. With increasing the depth, the nuclear and electronic energy losses decrease at the end of ion range. The sputtering rate value is large and it is about 2.6 atoms/ion.

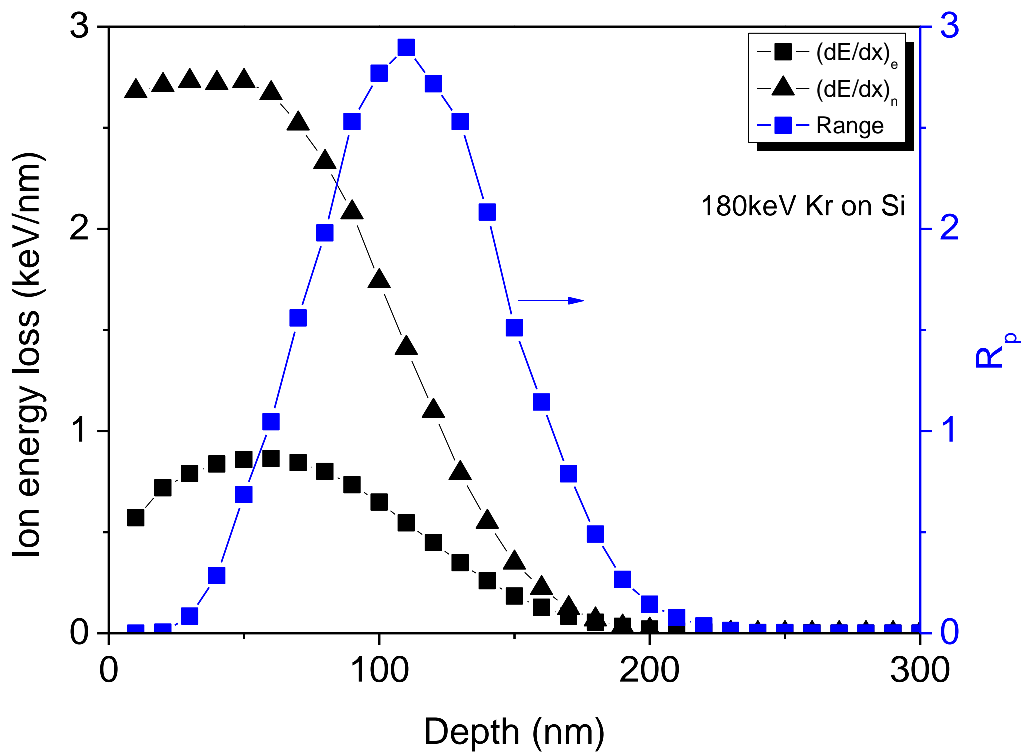

Figure 6-2. Electronic and Nuclear energy loss of 180 keV Kr ion, and the

projection range of the same irradiated condition calculated by SRIM 2008.

6.2 Annealing results

The annealed characteristics of swelling height were studied by irradiated samples (5 $\times 10^{15}$, 4 $\times 10^{16}$ and 8$\times 10^{16}$ atoms/cm^2), and the annealing temperatures are from 200 to 800 ℃ in Fig. 6-3. In the 5 $\times 10^{15}$ atoms/cm^2, the swelling height is reduced tendency. At annealing temperature up to 400 ℃, it still keeps the swelling height, but the swelling height reduces up 600 ℃. The swelling height nearly returns to original surface at 800 ℃. In the 4 $\times 10^{15}$ and 8 $\times 10^{16}$ atoms/cm^2, the swelling heights almost remain constant in the tendency. The different variations of swelling heights perform the low and high fluence irradiation. Because there is no interaction between the irradiated Kr ions and Si atoms, the reason of the variation may be the different damage effect in the samples. The Kr ions can produce larger number of dpa than Ar and He ions [46], but the swelling height is lower than Ar ions (~ 39.6 nm) [63] and He ions (~ 10 nm) [64] induced the swelling height by same conditions (fluence = 6 $\times 10^{16}$/cm^2). The reason must be the sputtering effect reduces the swelling silicon surface.

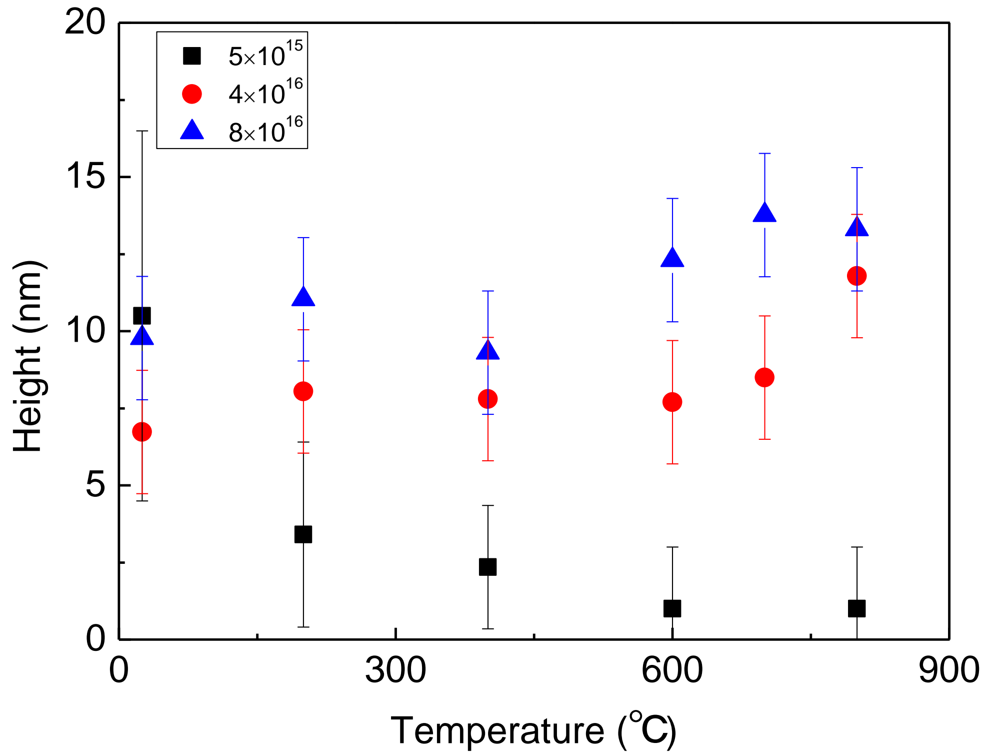

Figure 6-3. Swelling heights of annealed Kr irradiated Si samples as a function of various temperatures.

The helium ion irradiated and annealing in Si target, this situation is illustrated schematically for low fluence and high fluence irradiated silicon. For high fluence, defects do not collapse in extended interstitial type defect. Indeed, the void formation involves dissolution of interstitial type secondary defects [64]. Base on this theory, the annealed Si samples irradiated by high fluence Kr ions may change to secondary defects, so the swelling height almost constant at high temperature annealing. The irradiated by low fluence sample, it is recrystal during the annealing process, and then the surface becomes shrink.

6.3 Modification of lattice structure of Si crystal observed by Raman spectroscopy

The irradiated and annealed Si samples were measured by Raman spectrascopy at room temperature. Fig. 6-4 shows the Raman spectra of crystal Si, which was irradiated samples with fluence $0.5 \times 10^{15} \sim 8 \times 10^{16}$ atoms/cm^2 by 180 keV. The main variation of the optical phonon is related peak (1TO) [65-67]. The Si crystals (c-Si) induce a peak position at 520 cm^{-1} by 1TO phonon, and the amorphous Si (a-Si) causes about 480 cm^{-1} peak position by 1TO phonons [68, 67]. The second order acoustic photon mode (2TA) from c-Si causes 302 cm^{-1} peak position. After ion irradiation, the c-Si peak (520 cm^{-1}) disappears and arises a broad a-Si appears at about (480 cm^{-1}). This results indicates that irradiated samples transfer into a-Si in the excitation of light (532 nm Raman shift) penetrates depth during these fluence range, which reflect a large number of disorder Si atom in the irradiated layer.

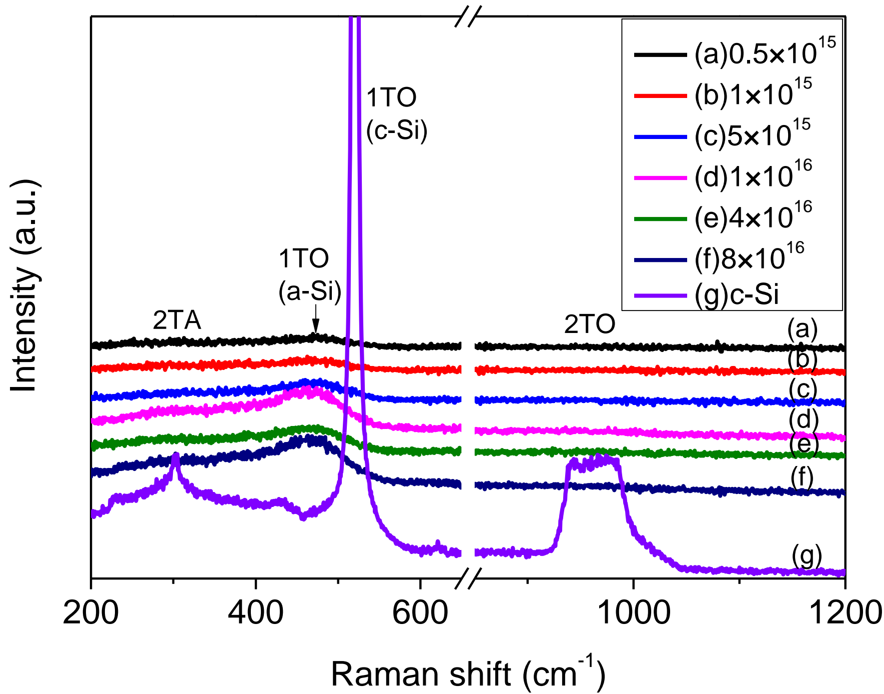

Figure 6-4. Raman spectra of Si sample irradiated Si by 180 keV Kr^{2+} ions with fluence $0.5 \times 10^{15} \sim 8 \times 10^{16}$ atoms/cm^2. The Raman spectrum of c-Si is shown as a reference.

Raman spectra of Si sample, which were annealed, are shown in Fig. 6-5. The sample irradiated by fluence 4×10^{16} atoms/cm^2 was annealed at the temperature range of 200 ～ 800 ℃. The crystalline peak is appear at 600 ℃, and continues enhancing up to 800 ℃. Raman spectra to detected nano/micro crystalline silicon often appear at 490-515 cm^{-1} [69, 70]. In the sample annealed at 600 ℃, the peak appears at about 495 cm^{-1}, and it proves nanocrystalline Si in the amorphous layer. According to these results, it is estimated that the thermal process that reduces Si amorphous damage induced by ion beam irradiation. Caused by this effect, the nanocrystalline of Si in the amorphous layer may re-grow to larger size nanocrystalline, which should be a mixed phase of nanocrystalline and amorphous

silicon in the irradiated layer as shown in the inset of Fig. 6-5. The blue shift of optical phonon peak could be explained by complex compressive stress, associated with the removal of crystal defect during annealing process [71, 72].

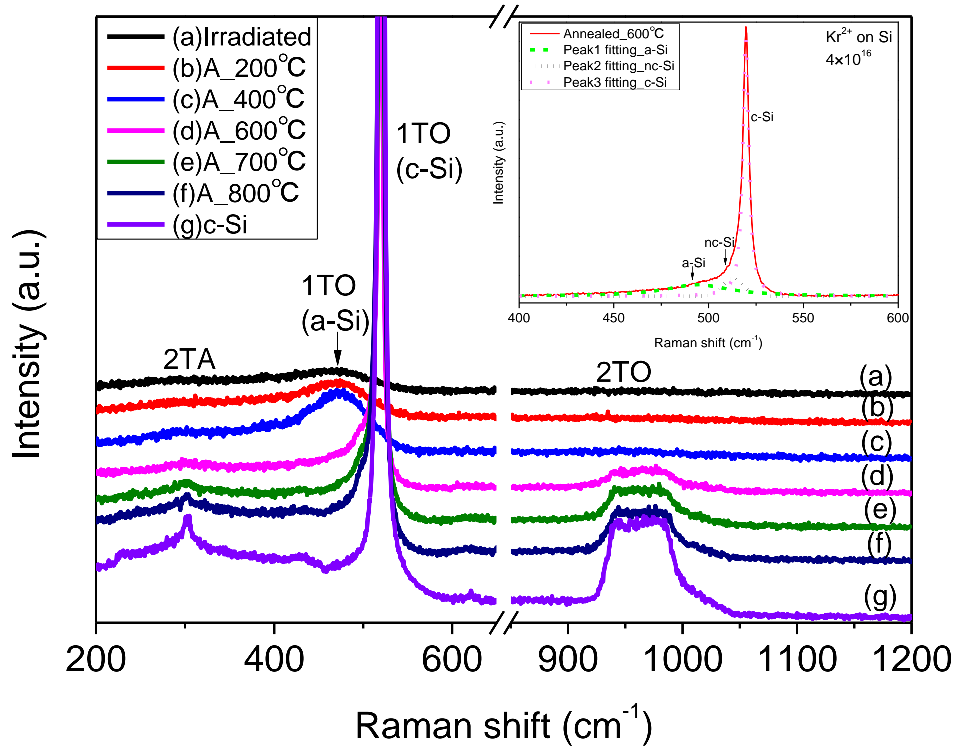

Figure 6-5. All of spectra measured at room temperature. Raman spectra of annealed Si samples in the temperature range 200 ～ 800℃.

The modification of swelling height induced by annealing process suggests the contribution of size change of nanocrystalline indicated by Raman spectroscopy: After irradiation, the crystalline Si is modified to amorphous Si. In the irradiated samples, there are amorphous and nanocrystalline Si phases in the irradiated layer during fluence 0.5×10^{15} atoms/cm^2 ～ 8×10^{16} atoms/cm^2. The size of nanocrystalline decreases with the irradiation fluence [73], while the swelling height

increases with the fluence in the experiment.

According to the above discussion, it is indicated that the annealing process, high temperature induces recrystallization of amorphous layer, which is formed by ion beam irradiation. In the annealing temperature up to 400 ℃, the a-Si peak corresponds to nanocrystallites. The nanocrystalline grows and the c-Si peak appears annealed at 600 ℃. By case of a sample irradiated 0.5×10^{15} atoms/cm^2, the swelling height decreases with the annealing process from 200 to 800 ℃. This is shown the decreasing behavior observed in the swelling height of the surface shrink during the annealing process. The increasing of the nanocrystalline size corresponds the decreasing of the defect in the amorphous Si. This phenomenon may contribute to the decrease of surface swelling height. In case of higher fluence, the swelling height is almost constant with annealing temperature from 200 to 800 ℃. The increasing of the nanocrystalline size, which can provide decreasing of the defect in the a-Si, but the irradiated samples by high fluence can not recover up to annealing temperature 800 ℃. There is still the amorphous peak in the annealed sample.

6.4 Modification of the surface roughness induced by annealing process

In this section, the surface morphology of annealed Si sample irradiated by Kr beam is described. Fig. 6-6 shows the surface morphology of Si samples irradiated with the fluence of 8×10^{16}/cm^2 and annealing at the temperature from 400 to 1000 ℃. Small bump structures start appearing on the surface annealed at 600 ℃. After the

annealing at 800 ℃, some small pits appear on the surface. The rms roughness is provided from morphological data, and data on the area 100 μm^2 is shown in Fig. 6-7. The results reveal modification of surface roughness depending on the annealing temperatures. The sudden increasing in rms rough at 1000 ℃ is caused by the formation of a lot of bump structures.

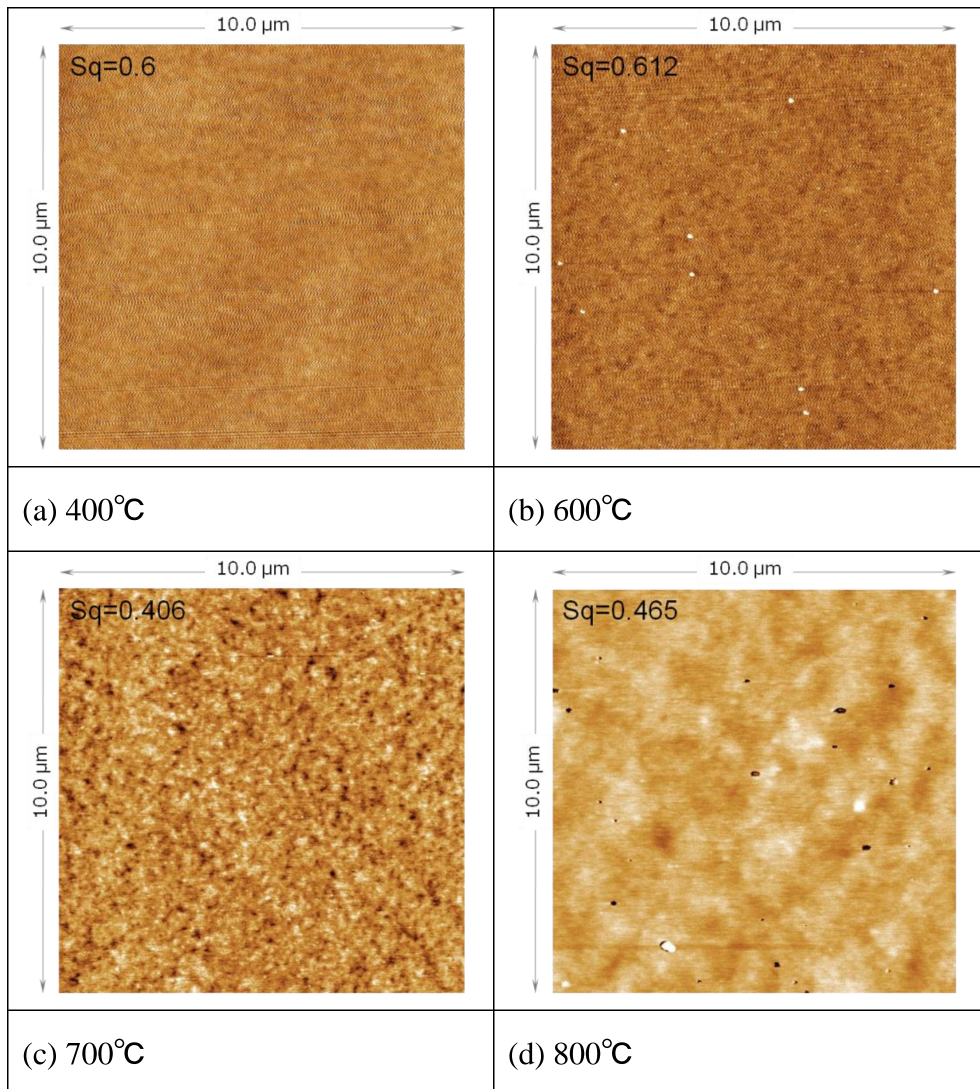

(a) 400℃ (b) 600℃

(c) 700℃ (d) 800℃

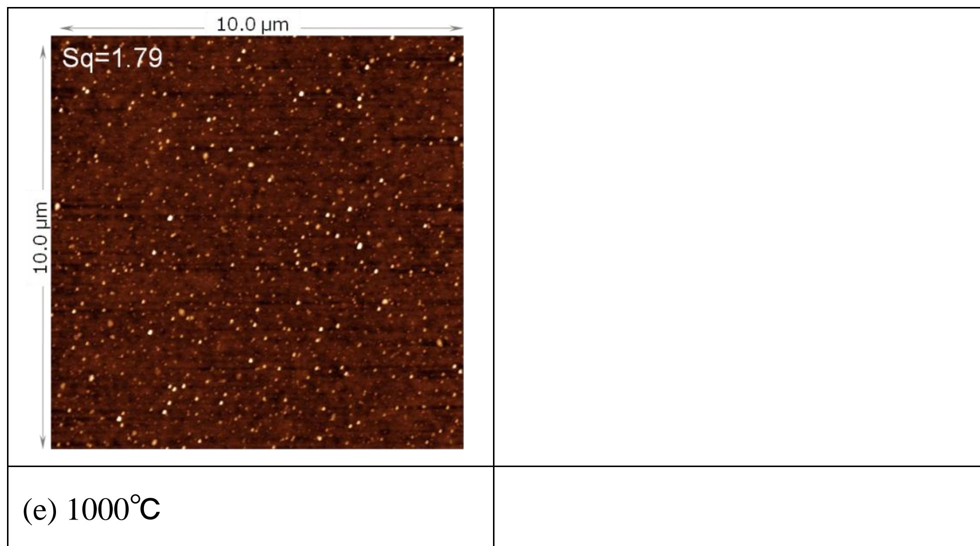

(e) 1000℃

Figure 6-6. Modification of surface morphology induced by annealing. AFM images of Si sample by 180 keV with fluence 8×10^{16} atoms/cm^2 are shown in (a-e).

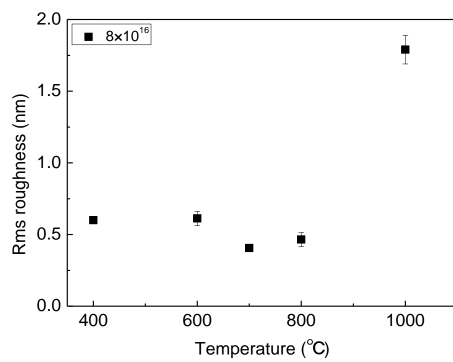

Figure 6-7. RMS roughness as a function of annealing temperature.

Chapter 7. Fabrication of Si surface pattern by Ar beam irradiation and annealing method

7.1 Definition of the crater structure

The typical surface pattern, fabricated by Ar-beam irradiation and a thermal annealing, is shown in Fig. 7-1. The figures show successive fabrication of crater structures on Si crystal. The diameter of crater structures was evaluated by FE-SEM image as shown in Fig. 7-1(a), and the depth of crater was measured by AFM as shown in Fig. 7-1(b). The average and standard deviation of a diameter and a depth were calculated from several craters, which were fabricated under same condition. According to the previous studies [74], the fabrication of crater is explained by an exfoliation arising from accumulated stress induced by irradiation.

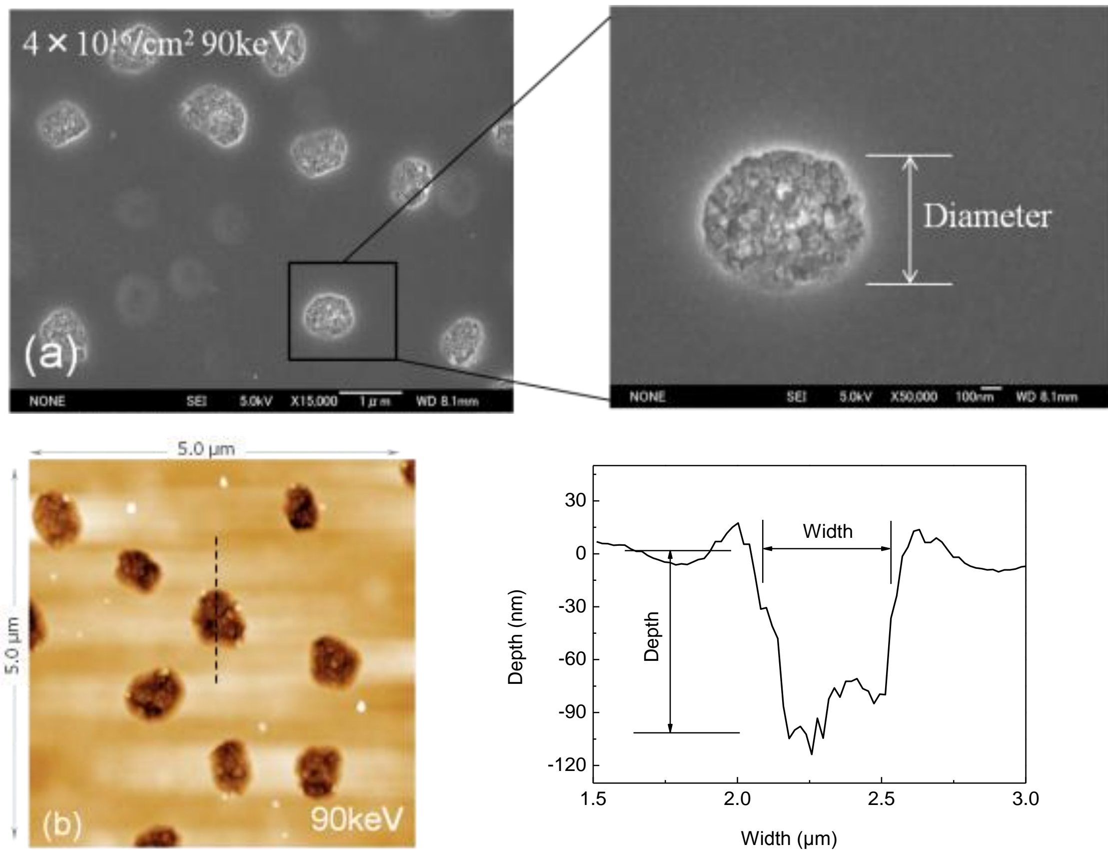

Figure 7-1. Typical surface pattern fabricated by Ar beam irradiation and annealing method. The FE-SEM (a) and AFM (b) images are used to determine diameter and depth.

7.2 Fluence dependence

According to observation, the fabricated crater pattern grows with a fluence of Ar-beam as shown in Fig. 7-2. The Fig. 7-2 shows the boundary between irradiated and un-irradiated region. An energy of Ar-beam is fixed at 90 keV, and the fluence varied in a range of 1 ~ 10 $\times 10^{16}/cm^2$. After the irradiation, a thermal annealing was performed. The crater pattern does not appear on the surface of Si target, which was irradiated with a fluence of 1 $\times 10^{16}/cm^2$, as shown in Fig. 7-2(a). The crater patterns suddenly appeared on the surface at the fluence of 4 $\times 10^{16}/cm^2$ as shown in Fig.

7-2(b). Fig. 7-2 also shows that the crater pattern becomes dense for the samples with higher fluence. The density of crater increases with the irradiation fluence.

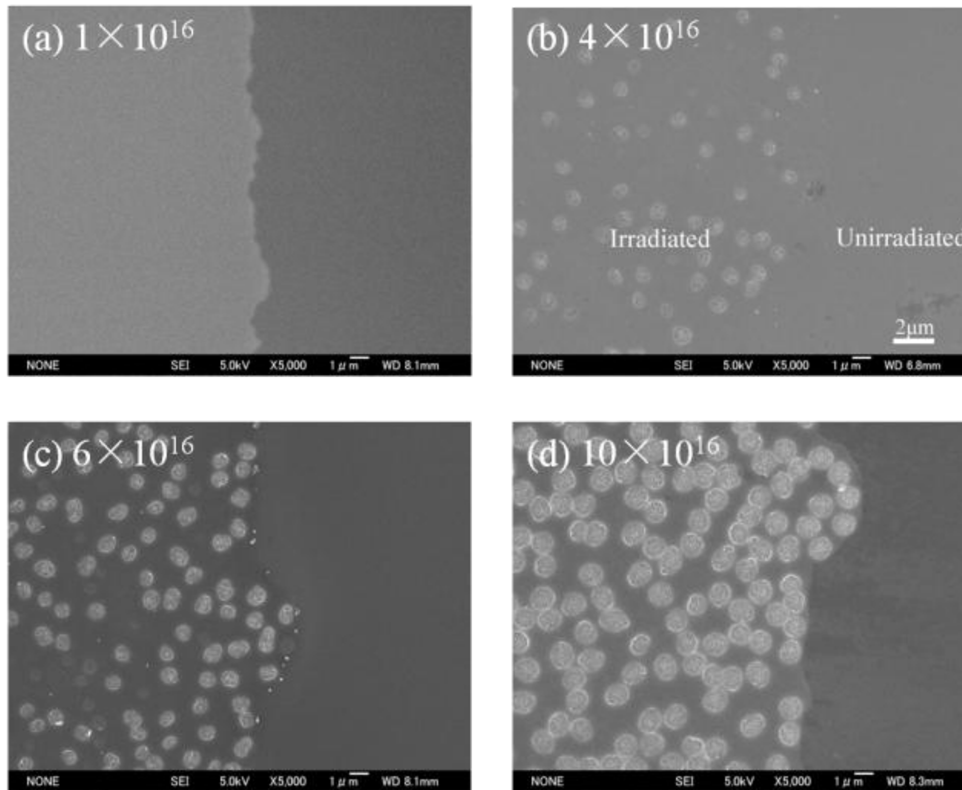

Figure 7-2. Growth of crater pattern on Si-crystal by increasing a fluence of Ar-beam observed by FE-SEM. The energy of Ar-beam was fixed at 90 keV.

The fluence dependence of a density and a diameter of crater fabricated on Si crystal are shown in Fig. 7-3. The density of crater is defined to be the number of craters in an area of 100 μm^2. In the present result, the crater density shows a remarkable increasing with the fluence as shown in Fig. 7-3(a). The threshold fluence to appear the crater structure sits between $1 \times 10^{16}/cm^2$ and $4 \times 10^{16}/cm^2$, and the density increases at higher fluence. On the other hand, the diameter of the craters is

observed to be almost constant (~ 0.8 μm) within its precision, as shown in Fig. 7-3(b).

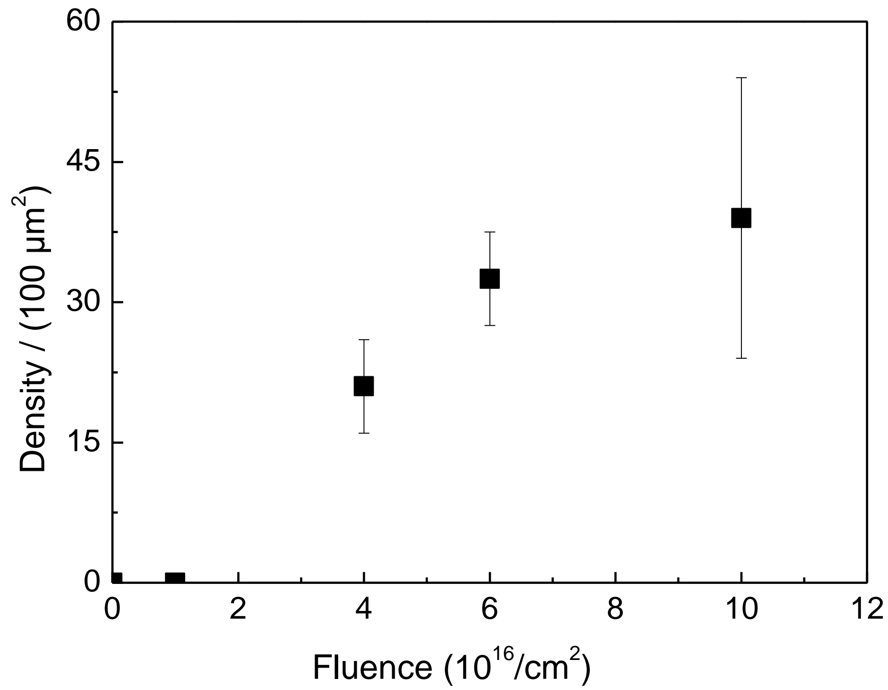

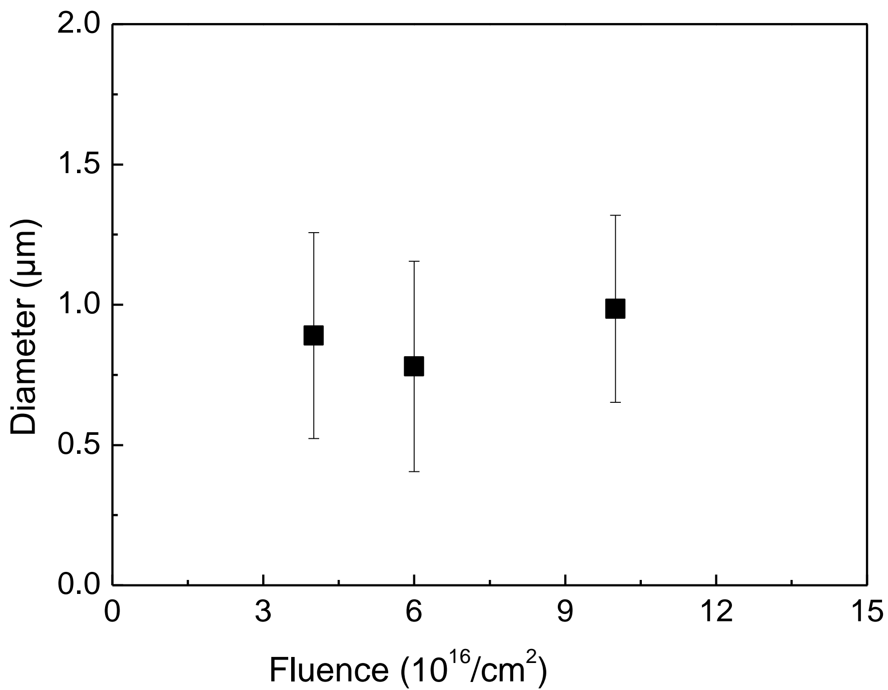

Figure 7-3. Density /100 μm^2 and diameter of crater as a function of fluence.

Therefore, it can be mentioned that the fluence is one of important parameters to control the density of the crater. This behavior may be explained based on the ion-beam induced stress in the irradiated crystal. According to ref [12], the internal stress, induced in crystal materials, increases with irradiated ions. Therefore, it is expected that the density of craters increases during annealing process.

7.3 Energy dependence

The fluence of Ar-beam is fixed at $4 \times 10^{16}/cm^2$, and the energy is varied between 90 and 270 keV. After the irradiation, a thermal annealing was performed. T The crater patterns, fabricated by Ar-beam with three different beam energies, are shown in Fig. 7-4. Fig. 4 shows drastic change in crater size corresponding to an energy of Ar-beam.

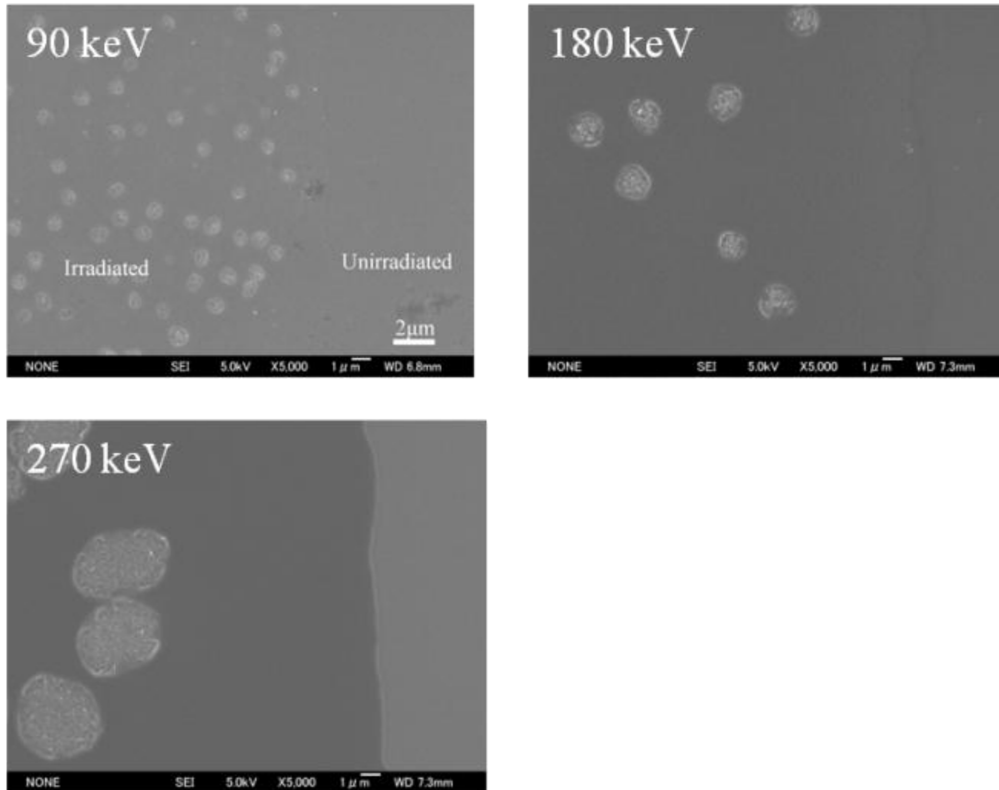

Figure 7-4. FE-SEM images of irradiated and unirradiated regions taken by various energies with fixed fluence 4 $\times 10^{16}$/cm^2 and annealed 600 ℃.

The energy dependence of the diameter of crater, fabricated on Si crystal, is shown in Fig. 7-5. The diameter of crater shows remarkable increase with Ar-beam energy. In the present result, the diameter increases from about 0.8 to 4.0 μm with beam energy range from 90 keV to 270 keV..

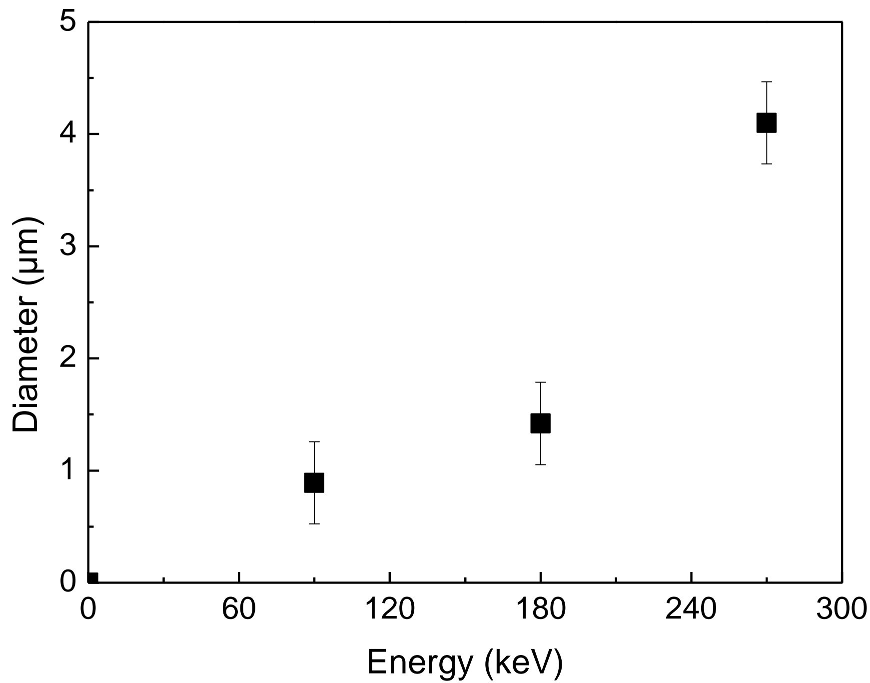

Figure 7-5. The diameter distribution of the crater by various energies with fluence 4×10^{16}/cm^2.

Fig. 7-6 shows three-dimensional profile of Si surface fabricated with an energy over a range of 90 ~ 270 keV and fixed fluence of 4×10^{16}/cm^2. A diameter and a depth of crater structures are obtained from the cross-section. In addition, cross-sections in Fig. 6 show rough structures on a bottom of craters. In the previous studies [75, 38], the formation of crater structure is understood based on an exfoliation of surface modified by ion beam. Therefore, it is evaluated that the bottom is formed by the polysilicon.

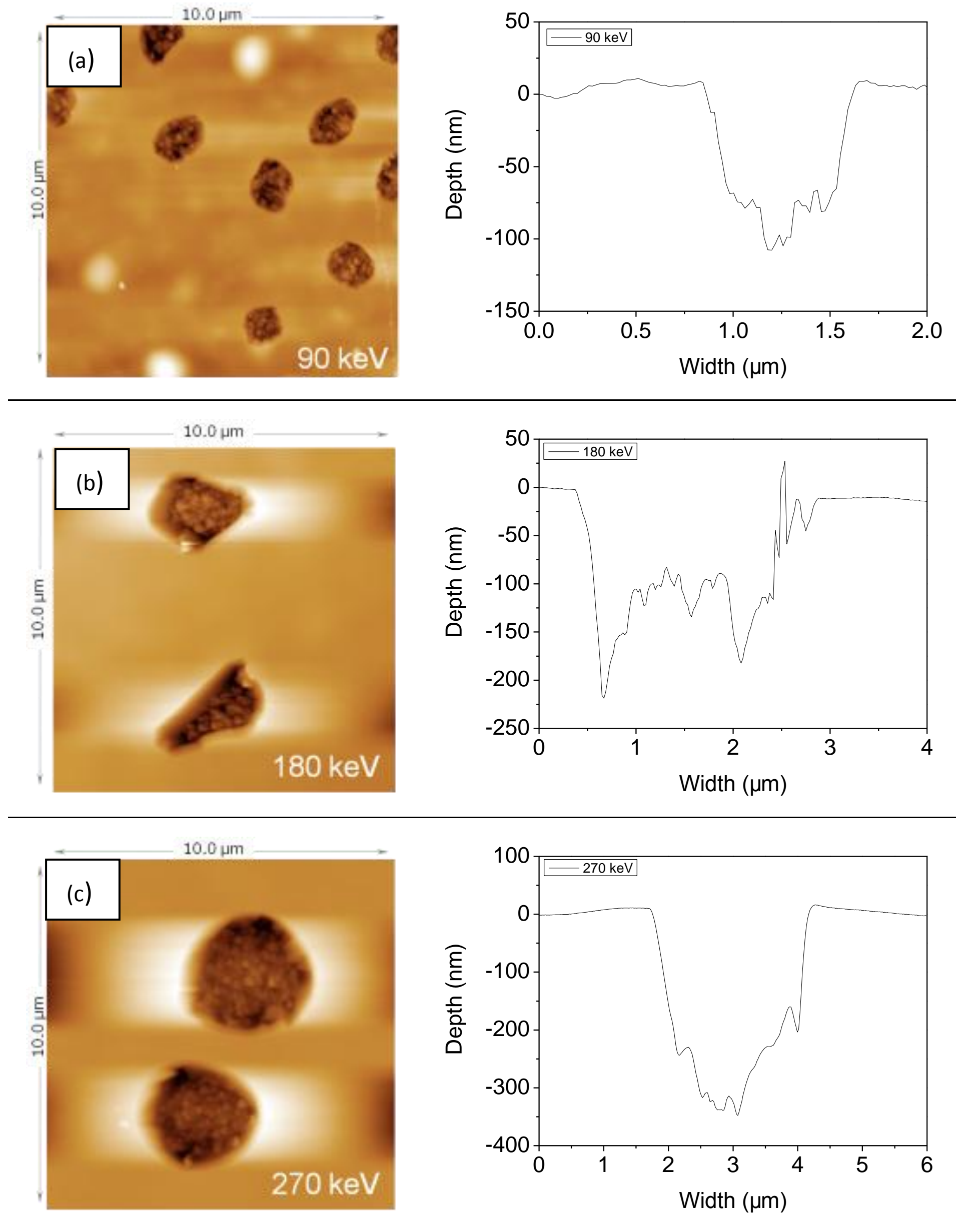

Figure 7-6. AFM measured surface information of crater structure by various energies. The typical line scans from the images are presented.

Fig. 7-7 shows the energy dependence of depth distribution of fabricated craters by Ar-beam in Si target. The depth of craters increases with the irradiation energy.

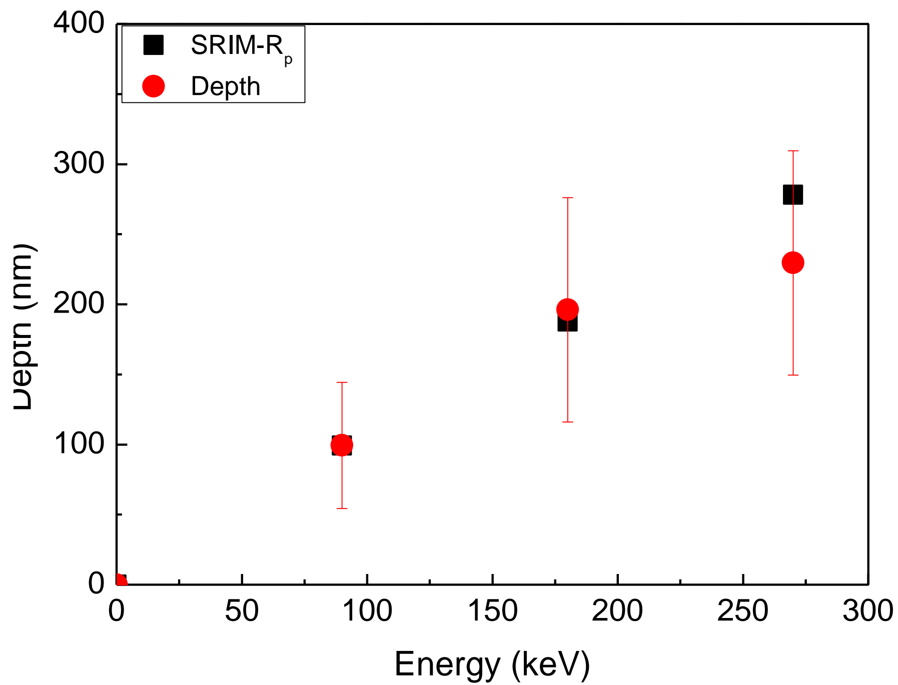

Figure 7-7. Depth distribution of craters and projection range (R_p) in Si as a function of beam energy.

Fig. 7-8 shows the range distribution of Ar beam in Si crystal, which is calculated by SRIM 2008 [46]. It can be seen clearly in the figure that the depth distribution expands with the beam energy proportionally. On the other hand, the maximum density decreases gradually with irradiation energy. The characteristic depth concerning a layer modified by Ar-beam irradiation is difined by means of the projection range (R_p).

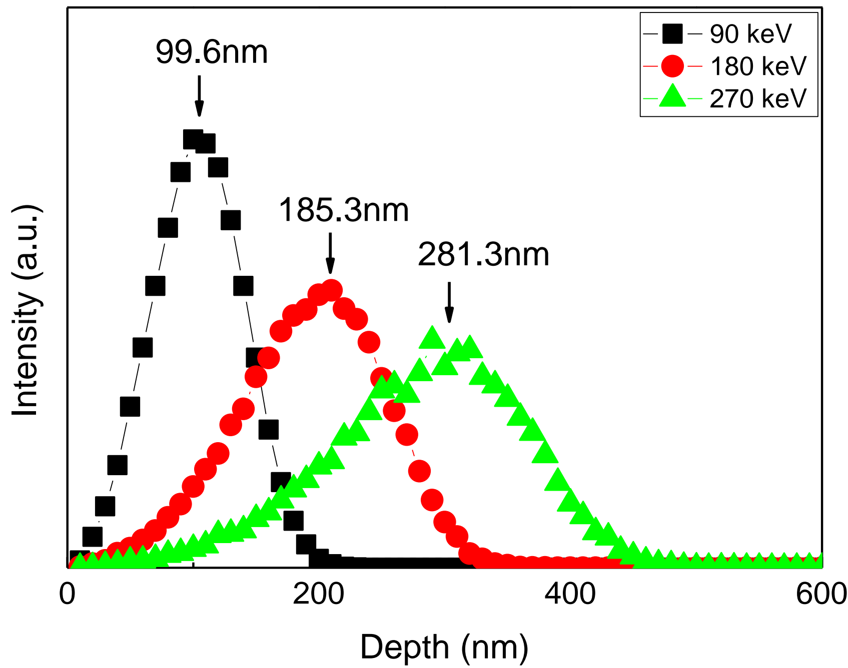

Figure 7-8. Depth distribution of projection range (R_p) of Ar-beam in Si crystal calculated by SRIM2008.

In these results of fluence and energy dependence, there exists a threshold fluence to form the crater structure. The increasing behavior of the density with the fluence of Ar beam is consistent with the exfoliation phenomenon observed by using H/He beams [76]. A diameter of craters is almost constant for different fluence, but an energy dependence diameter shows same increasing behavior with energy of Ar-beam. This may explain by the increasing the irradiation depth. The increasing behavior of crater depth of crater is almost consistent with calculated R_p as shown in fig. 7-7. It is means that the exfoliated position closes to the projection range layer to form the crater.

According to above discussion, the irradiation fluence is an important parameter to control the crater density, and the irradiation energy is an important parameter to

control the crater diameter and depth. In our experiment, we use the rare gas-Ar beam irradiation. There is no chemical interaction by the Ar-beam irradiated and annealed Si target, which is different with the irradiated from Hydrogen-beam [77, 78].

7.4 The comparison with previous data

In the previous studies, the depths of crater structure produced by irradiated ions (Ar, He+H, H_2 and H) on Si target were observed and the results are shown in Table.7-1. The projection ranges (R_p) are calculated by SRIM 2008 (full cascade simulations) for various ions irradiation. To look for general behavior of the crater depth on the R_p, the fitting line of all the data is shown in Fig. 7-9. In the equation of the depth is plotted as a function of R_p, and the slop of the fitting line is about 1. The experimental data is almost constant tendency of the crater depth by the different ion irradiation, so it may be independent of the irradiation ions.

Table 7-1. Depth of craters fabricated by different ions and the projection range (R_p) calculated by SRIM 2008[46] on the Si target.

Ion	Target	Fluence ($10^{16}/cm^2$)	Energy (keV)	Projection range (R_p)	Depth (nm)
Ar	Si <100>	4	90	96.6	99.4
Ar	Si <100>	4	180	185.3	196.1
Ar	Si <100>	4	270	281.3	229.6
He/H	Si (100)	3/2	30/24	282.0/275.1	>282 [79]
He/H	Si (100)	5/1	160/110	921.9/955.0	960 [38]
H_2^+	Si (001)	4	5 (15°)	75	72±5 [15]
H	Si (100)	1	10 (30°)	134.2	100 [16]
H	Si (001)	5	15	181	249 [80]

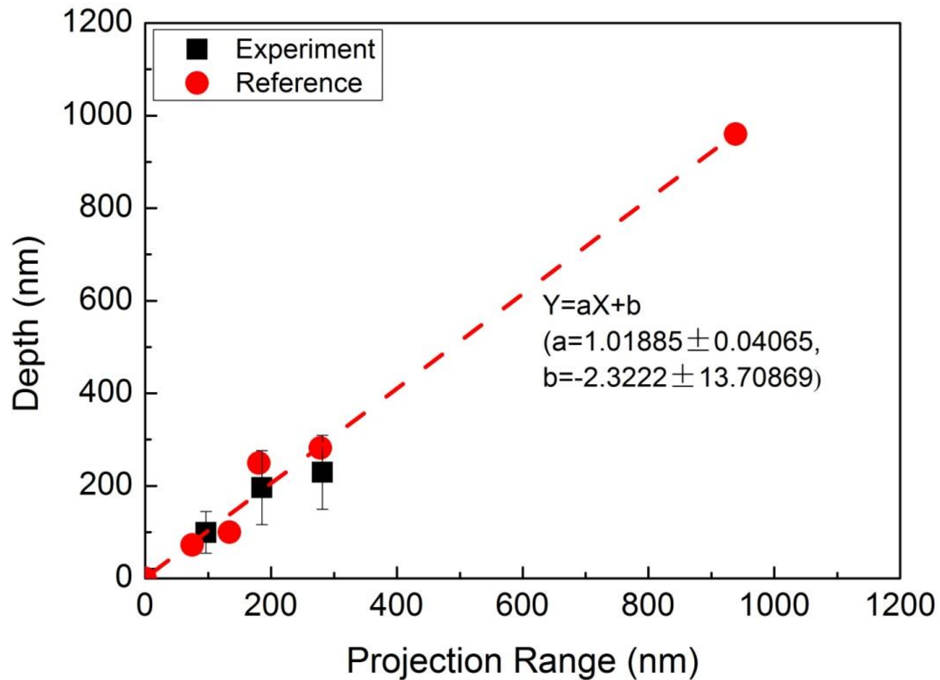

Figure 7-9. Depth of crater as a function of projection ion range (R_p) on the Si target. The experimental data and references are shown with symbols, while the line represents a linear fit to the data.

The cross section information of irradiated Si at 90 keV is shown in Fig. 7-10. The TEM image clearly shows that the crater structures come from the exfoliation of the Si over layer. The bottom of crater is close to the interface between the irradiated layer and crystal Si. The composing of depth of crater should be considered as the swelling height irradiated by Ar beam. No bubbles or voids were observed by cross-sectional transmission electron microscopy.

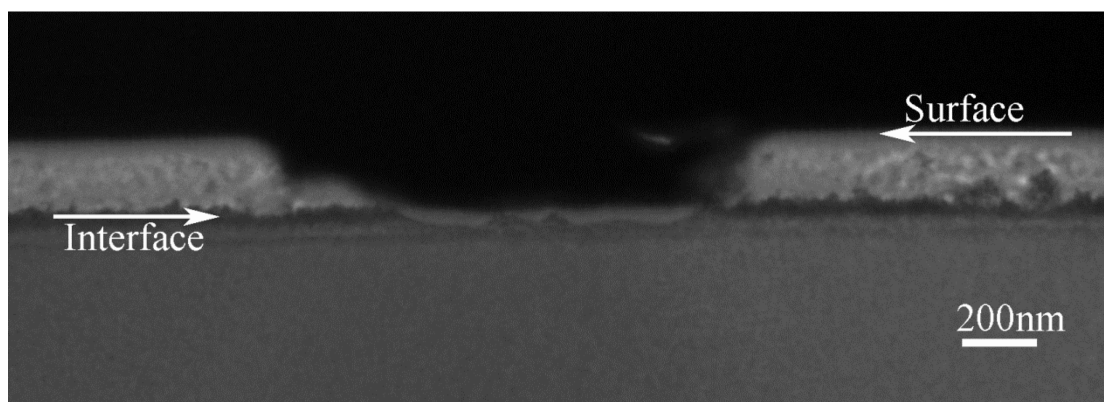

Figure 7-10. Low magnification cross-sectional TEM bright-field images from the surface crater region, viewed edge on in the single crystal <100> silicon wafer. The Si sample was Ar-ion- irradiated under room temperature with 4×10^{16} H/cm^2 by 90 keV and annealed 600℃.

The density of the crater structure has a strong relationship with the irradiation fluence. There is a threshold fluence to form the crater structure in this experimental condition. The density increases with the fluence, which agrees with H and He beam induced the surface exfoliation phenomenon [76]. The diameter is almost constant in the uniform energy which may explain the irradiated same the projection range. The surface diameters are enlarged, when we increase the irradiation energy in the fluence 4×10^{16}/cm^2. The irradiation energy is an important parameter to control the crater diameters. The depth of crater increase with the irradiation energy, and the deepest position closes to the interface of the irradiated layer. The tendency of the crater depth is independence of irradiated ions, and it may depend on type of the target. It appears that the diameter, density and morphology of crater pattern depend on the irradiated fluence and energy. There is no chemical interaction by the Ar ions

irradiated and annealed Si target, which is different with the irradiated from hydrogen ions [77, 78].

8. Conclusion

In this thesis, we studied about fabrication of the 3-D structure along vertical direction. Fabrication method of swelling and crater structure which were investigated in this thesis, are found to be the simple methods to control the vertical direction. This study has strongly indicated the feasibility of swelling and crater method as a fabrication technique of 3-D structure on Si crystal. The major results are summarized as following:

1. Control of Swelling Height of Si Crystal by Irradiating Ar Beam

We could fabricate the various swelling height by changing three parameters (fluence,charge and energy). The swelling height increases with the fluence monotonously. The swelling height also increased with the acceleration energy of Ar ions up to 400 keV. Base on the above results, it was confirmed that the swelling height can be controlled by three parameters. We assumed that the swelling height depends on the behavior of ion-beam induced defect in Si crystal. Based on the idea, these observed results are well understood by the amount of ion-beam induced defect simulated from SRIM. By comparing with previous results, we have shown the possibility to control the swelling height by changing ion irradiation. In addition, it is found that the swelling height is stable at room temperature. All these results indicate this method of producing swelling structure indicates the potential application to fabricate 3-D nanostructure.

2. Swelling and annealing phenomena of Si crystal irradiated by Ar and C ion beams

The swelling height of Si crystal, induced by Ar^+ and C^+ ion beam, and its modification through post-irradiation annealing process have been observed. Based on experimental results, the mechanism of swelling and annealing phenomena has been discussed. The different features, observed for between Ar^+ and C^+ ion beams, were understood by means of damage induced in Si crystal, which is evaluated by using. Because of larger nuclear collision power of Ar beam compared with C beam, Ar beam have higher productivity of ion-beam induced damage in Si crystal under the same irradiation condition. Higher swelling height observed for Ar beam is understood the difference in the productivity of damage. In case of Ar beam, the damage induced in Si crystal is amorphous phase of Si, voids and small bubbles. In case of C beam, the damage induced in Si crystal is amorphous phase of Si and $Si_{1-x}C_x$ alloys and a minor component of SiC, which would provide small contribution for volume expansion. The different features were also observed in annealing process for Si crystals. The swelling height of the Ar irradiated Si crystal showed sudden increase at 600 ℃, and a small increase of the height occurred at 800 ℃. On the other hand, the swelling height of C irradiated Si crystal showed sudden decrease at 600 ℃ and was almost disappeared at 800 ℃. It is implied that the different annealing features would be understood by means of rearrangement process for amorphous phase of Si, which is almost recrystallized at 800 ℃. Ar atom could exist in Si crystal as bubbles, which can change their size corresponding to

temperature. The swelling height would increase with increasing bubble sizes and outward diffusion processes. In case of C ion beam, irradiated C atoms would diffuse, and forms $Si_{1-x}C_x$ amorphous alloys at high temperatures. The phase transfer from amorphous to crystal would cause the reduction in volume at the swelling area. The morphological modification, induced by annealing, is a good index to study the crystal swelling phenomenon and mechanism. It is needed to get the cross sectional modification of the irradiated region for further study of swelling mechanisms in detail.

3. Experimental study on the mechanism of Si swelling phenomenon by Kr beam

The swelling height of Si was studied by irradiating Kr ion with various fluence of $0.5 \times 10^{15} \sim 8 \times 10^{16}$ atoms/cm^2. Following the irradiation process, annealing method was applied to study the change of swelling height within the temperature range of 200 ～ 800 ℃. The modification of swelling height, induced by annealing process, shows different behaviors corresponding to irradiation fluence. The damage induced in Si crystal was evaluated by Raman spectra before and after the irradiation and annealing process. The Raman spectra have confirmed the recrystallization of ion beam induced defect by means of thermal annealing process. According to the results, the recrystallization has started at 600 ℃, and there remains the phase of nanocrystalline and amorphous silicon in the irradiated layer. The Raman spectrum gave us useful information to explain the swelling mechanism in the irradiated target. The roughness of irradiated surface becomes roughness and the RMS value is up to

about 1.79 nm as annealing temperature at 1000 ℃.

4. Fabrication of Si surface pattern by Ar beam irradiation and annealing method

In this paper, we have studied about simple method to fabricate surface crater, which consists of Ar-beam irradiation and a thermal annealing at 600 ℃. The crater pattern by means of fluence and energy of Ar-beam. The density of the craters have varied in a range of 0 ~ 39 /100μm^2 by changing fluence. By changing energy of Ar-beam, the diameter and depth of the craters have varied in a range of 0.8 ~ 4.1 μm and 99 ~ 229 nm, respectively. It is expected that the rare gas irradiation method does not bring additional chemical reaction and obvious chemical bond. The chemical property can be kept by rare gas irradiation, which may give an additional and useful choice in the field of 3-D structure fabrication.

Acknowledgement:

I would like to thank Professor Momota sadao, my supervisor, for his guidance and support during my PhD period. Thank you for giving me freedom in doing research and teaching me the research methods.

This irradiation experiments were supported by Momota-Lab colleagues. (T. Toyonaga, F. Imanishi, K. Maeda, H. Terauchi, H. Fukui, H. Katou, Y. Hashimoto, X. Guo, S. Shinnyama)

Analysis results of Raman, AFM and TEM were helped by Prof. M. Furuta, Dr. T. Kawaharamura, Dr. N. Nitta. Dr. D. Wang et al.

Discussions and suggestions of Prof. M. Taniwaki, Prof. M. Furuta, Prof. T. Tsuji, Prof. H. Fruta.

I appreciate all IRC staff members to make my staying in Japan comfortable, enjoyable, and memorable.

Thanks all my friends at KUT. At last, I would like to thanks my family members.

References:

[1] M. Elwenspoek, H.V. Jansen, 1998 Silicon Micromachining (Cambridge: Cambridge University Press).

[2] D. Bratton, D. Yang, J. Dai, C.K. Ober, Polymers for Advanced Technologies 17 (2006) 94-103.

[3] P.E. Russell, T.J. Stark, D.P. Griffis, J.R. Phillips, K.F. Jarausch, J. Vac. Sci. Technol. B 16 (1998) 2494.

[4] S. Matsui, K. Kaito, J. Fujita, M. Komuro, K. Kanda, Y. Haruyama, J. Vac. Sci. Technol. B 18 (2000) 3181.

[5] N. Kawasegi, N. Morita, S. Yamada, N. Takano, T. Oyama, S. Momota, J. Taniguchi, I. Miyamoto, Applied Surface Science 253 (2007) 3284-3291.

[6] J. Orloff, M. Utlaut, L. Swanson, High-resolution Focused Ion Beams (Kuluwer Academic/Plenum Publishers) (New York, 2003).

[7] N.N. Berchenko, V.V. Bogoboyashchiy, I.I. Izhnin, M. Pociask, E.M. Sheregii, V.A. Yudenkov, Physica Status Solidi (c) 2 (2005) 1418-1422.

[8] J.S. Custer, M.O. Thompson, D.C. Jacobson, J.M. Poate, S. Roorda, W.C. Sinke, F. Spaepen, Appl. Phys. Lett. 64 (1994) 437.

[9] R. Nipoti, E. Albertazzi, M. Bianconi, R. Lotti, G. Lulli, M. Cervera, Appl. Phys. Lett. 70(25) (1997) 3425-3427.

[10] M. Ikeyama, K. Saitoh, S. Nakao, H. Niwa, S. Tanemura, Y. Miyagawa, S. Miyagawa, 1998 International Conference on Ion Implantation Technology

Proceedings 2 (1999) 736-739.

[11] P. Giri, V. Raineri, G. Franzo, E. Rimini, Phys. Rev. B 65 (2001) 012110.

[12] C. Trautmann, M. Boccanfuso, A. Benyagoub, S. Klaum€unzer, K. Schwartz, M. Toulemonde, Nucl. Instr.Meth.Phys.B 191 (2002) 144-148.

[13] Y.H. Li, Y.Q. Wang, J.A. Valdez, M. Tang, K.E. Sickafus, Nuclear Instruments and Methods in Physics Research Section B: Beam Interactions with Materials and Atoms 274 (2012) 182-187.

[14] A. Markwitz, V.J. Kennedy, H. Baumann, Nucl. Instr. and Meth. in Phys. Res. B 206 (2003) 179-183.

[15] A. Giguère, J. Beerens, B. Terreault, Nanotechnology 17 (2006) 600-606.

[16] S. Igarashi, A.N. Itakura, M. Kitajima, Jpn. J. Appl. Phys. 46 (2007) 7812-7815.

[17] M. Rudolphi, A. Markwitz, H. Baumann, Surface and Interface Analysis 39 (2007) 698-701.

[18] W.G. Spitzer, G.K. Hubler, T.A. Kennedy, Nucl. Instr. and Meth. in Phys. Res. B 209-210 (1983) 309-312.

[19] F. Yongqi, N. Kok, A. Bryan, N.P. Hung, O.N. Shing, Rev. Sci. Instrum. 71 (2000) 1006.

[20] G.C. Gazzadi, P. Luches, S.F. Contri, A. di Bona, S. Valeri, Nuclear Instruments and Methods in Physics Research Section B: Beam Interactions with Materials and Atoms 230 (2005) 512-517.

[21] C.G. Lee, Y. Takeda, N. Kishimoto, N. Umeda, J. Appl. Phys. 90 (2001) 2195.

[22] H. Huber, W. Assmann, S.A. Karamian, A. Mücklich, W. Prusseit, E. Gazis, R.

Grötzschel, M. Kokkoris, E. Kossionidis, H.D. Mieskes, R. Vlastou, Nucl. Instr. and Meth. in Phys. Res. B 122 (1997) 542-546.

[23] R. Callec, A. Poudoulec, J. Appl. Phys. 73 (1993) 4831.

[24] D.L. Williamson, S. Roorda, M. Chicoine, R. Tabti, P.A. Stolk, S. Acco, F.W. Saris, Appl. Phys. Lett. 67 (1995) 226.

[25] P. Giri, Materials Science and Engineering B 121 (2005) 238-243.

[26] J.F. GIBBONS, Proc. IEEE 60 (1972) 1062-1096.

[27] J.R. Dennis, E.B. Hale, J. Appl. Phys. 49 (1978) 1119.

[28] K.F. Heidemann, Phil. Mag. 44 (1981) 465-485.

[29] J.K.N. Lindner, R. Domres, E.H.T. Kaat, Nucl. Instr. and Meth. in Phys. Res. B 39 (1989) 306-310.

[30] H. Sirringhaus, T. Kawse, R.H. Friend, T. shimoda, M. Inbasekaran, W. Wu, E.P. Woo, Science 290 (2000) 2123.

[31] V.V. Poborchii, T. Toda, T. Kanayama, Appl. Phys. Lett. 75 (1999) 3276.

[32] A.J. Haes, R.P.V. Duyne, J. Am. Chem. Soc 124 (2002) 10596.

[33] M.D. Levenson, N.S. Viswanathan, R.A. Simpson, IEEE Trans. Electron Devices 29 (1982) 1828.

[34] W. Chen, H. Ahmed, Appl. phys. Lett. 62 (1993) 1499.

[35] S. Yasin, D.G. Hasko, H. Ahmed, Appl. Phys. Lett. 78 (2001) 2760.

[36] M. Bruel, ELECTRONICS LETTERS 31 (1995) 1201.

[37] L.-J. Huang, Q.-Y. Tong, Y.-L. Chao, T.-H. Lee, Appl. Phys. Lett. 74 (1999) 982.

[38] Z. Wang, C. Liu, T. Liu, X. Zhang, W. Li, W. Li, B. Yuan, P. Wu, M. Li, Nucl. Instr. and Meth. in Phys. Res. B 266 (2008) 250-255.

[39] W. Düngen, R. Job, Y. Ma, Y.L. Huang, T. Mueller, W.R. Fahrner, L.O. Keller, J.T. Horstmann, H. Fiedler, J. Appl. Phys. 100 (2006) 034911.

[40] http://www.el-cat.com/silicon-properties.htm.

[41] H. Ryssel, I. Ruge, 1986.

[42] S. Momota, Y. Nojiri, M. Saihara, A. Sakamoto, H. Hamagawa, K. Hamaguchi, Rev. Sci. Instr. 75 (2004) 1497.

[43] S. Iwamitsu, M. Nagao, S.A. Pahlovy, K. Nishimura, M. Kashihara, S. Momota, Y. Nojiri, J. Taniguchi, I. Miyamoto, T. Nakao, N. Morita, N. Kawasegi, Colloids and Surfaces A: Physicochemical and Engineering Aspects 313-314 (2008) 407-410.

[44] G. Binnig, C.F. Quate, C. Gerber, Phys. Rev. Lett. 56 (1986) 930-933.

[45] J. Yan, T. Asami, T. Kuriyagawa, Precision Engineering 32 (2008) 186-195.

[46] J.F. Ziegler, J.P. Biersack, M.D. Ziegler, The Stopping and Range of Ions in Matter, (SRIM Co., Chester, 2008), The Stopping and Range of Ions in Solids (Pergamon, New York, 1985), v. 1.321 pp.

[47] P. Schmuki, L.E. Erickson, G. Champion, B.F. Mason, J. Fraser, C. Moessner, Appl. Phys. Lett. 70 (1997) 1305.

[48] Y. Gao, J. Xue, D. Zhang, Z. Wang, C. Lan, S. Yan, Y. Wang, F. Xu, B. Shen, Y. Zhang, Journal of Vacuum Science & Technology B: Microelectronics and Nanometer Structures 27 (2009) 2342.

[49] L. Romano, G. Impellizzeri, M.V. Tomasello, F. Giannazzo, C. Spinella, M.G.

Grimaldi, Journal of Applied Physics 107 (2010) 084314.

[50] J.-P. Briand, G. Giardino, G. Borsoni, V.L. Roux, N. Béchu, S. Dreuil, O. Tüske, Rev. Sci. Instr. 71 (2000) 627.

[51] P.X. Zhang, I.V. Mitchell, B.Y. Tong, P.J. Schultz, D.J. Lockwood, Phys. Rev. B 50 (1994) 17080.

[52] U. Bangert, P.J. Goodhew, C. Jeynes, I.H. Wilson, J. Phys. D 19 (1986) 589-603.

[53] L.A. Marqués, J.E. Rubio, M. Jaraíz, L.A. Bailón, J.J. Barbolla, J. Appl. Phys. 81 (1997) 1488.

[54] L. Pelaz, L.A. Marqués, J. Barbolla, Journal of Applied Physics 96 (2004) 5947.

[55] M.W. Bench, I.M. Robertson, M.A. Kirk, I. Jenčič, Journal of Applied Physics 87 (2000) 49.

[56] S.-i. Satake, S. Momota, S. Yamashina, M. Shibahara, J. Taniguchi, J. Appl. Phys. 106 (2009) 044910.

[57] J.K.N. Lindner, Appl. Phys. A 77 (2003) 27-38.

[58] W. Skorupa, A. Yankov, Materials Chemistry and Physics 44 (1996) 101-144.

[59] M.V. Nguyen, K. Vedam, J. Appl. Phys. 67 (1990) 3555.

[60] H. Isogai, E. Toyoda, T. Senda, K. Izunome, K. Kashima, N. Toyoda, I. Yamada, Nucl. Instr. and Meth. in Phys. Res. B 257 (2007) 683-686.

[61] B. Li, C. Zhang, L. Zhou, Y. Yang, H. Zhang, Nucl. Instr. and Meth. in Phys. Res. B 266 (2008) 5112-5115.

[62] P. Werner, H.-J. Gossmann, D.C. Jacobson, U. Gösele, Appl. Phys. Lett. 73 (1998) 2465.

[63] S. Momota, J. Zhang, T. Toyonaga, H. Terauchi, K. Maeda, J. Taniguchi, T. Hirao, M. Furuta, T. Kawaharamura, J. Nanosci. Nanotechnol 12 (2012) 552.

[64] V. Raineri, S. Coffa, E. Szilágyi, J. Gyulai, E. Rimini, Phys. Rev. B 61 (2000) 937.

[65] A. Zwick, R. Carles, Phys. Rev. B 48 (1993) 6024-6032.

[66] M. Ehbrecht, B. Kohn, F. Huisken, M.A. Laguna, V. Pailland, Phys. Rev. B 56 (1997) 6958-6964.

[67] P. Mishra, K. Jain, Phys. Rev. B 64 (2001).

[68] J.E. Smith, Jr., M.H. Brodsky, B.L. Crowder, M.L. Nathan, A. Pinczuk, Physical Review Letters 26 (1971) 642-646.

[69] X.L. Wu, G.G. Siu, S.Tong, X.N. Liu, F. Yan, S.S. Jiang, X.K. Zhang, D. Feng, Appl. Phys. Lett. 69 (1996) 523-525.

[70] S. Momota, J. Zhang, T. Toyonaga, H. Terauchi, K. Maeda, J. Taniguchi, T. Hirao, M. Furuta, T. kawaharamura, J. Nanosci. Nanotechnol 12 (2012) 552-556.

[71] N. Fukata, T. Oshima, K. Murakami, T. Kizuka, T. Tsurui, S. Ito, Appl. Phys. Lett. 86 (2005) 213112.

[72] S. Mohanta, R. Soni, S. Tripathy, C. Soh, S. Chua, D. Kanjilal, Physica E 35 (2006) 42-47.

[73] V. Lavrentiev, J. Vacik, V. Vorlicek, V. Vosecek, physica status solidi (b) 247 (2010) 2022-2026.

[74] A.M. T. Höchbauer, M. Nastasi, J. W. Mayer, J. Appl. Phys. 92 (2002) 2335.

[75] J. Zahler, A. Fontcuberta i Morral, M. Griggs, H. Atwater, Y. Chabal, Physical Review B 75 (2007) 035309-035301.

[76] S. Reboh, A.A.D. de Mattos, F. Schaurich, P.F.P. Fichtner, M.F. Beaufort, J.F. Barbot, Scripta Materialia 65 (2011) 1045-1048.

[77] P. Nguyen, I. Cayrefourcq, K.K. Bourdelle, A. Boussagol, E. Guiot, N. Ben Mohamed, N. Sousbie, T. Akatsu, J. Appl. phys. 97 (2005) 083527.

[78] J.H. Liang, C.Y. Bai, D.S. Chao, C.M. Lin, Nucl. Instr. and Meth. in Phys. Res. B 266 (2008) 1349-1355.

[79] B.S. Li, C.H. Zhang, H.H. Zhang, Y. Zhang, Y.T. Yang, L.H. Zhou, L.Q. Zhang, Nucl. Instr. and Meth. in Phys. Res. B 268 (2010) 555-559.

[80] C. Coupeau, E. Dion, M.L. David, J. Colin, J. Grilhé, EPL (Europhysics Letters) 92 (2010) 16001.

Publication

Sadao Momota, Jianguo Zhang, Takuya Toyonaga, Hikaru Terauchi, Kazuki Maeda, Jun Taniguchi, Takashi Hirao, Mamoru Furuta, Toshiyuki Kawaharamura, J. Nanosci. Nanotechnol.12 (2012) 552

J. Zhang, S. Momota, T. Toyonaga, H. Terauchi, F. Imanishi, J. Taniguchi, Nucl. Instr. and Meth. in Phys. Res. B 280 (2012) 17

Jianguo Zhang, Sadao Momota, Hikaru Terauchi, Kazuki Maeda, Jun Taniguchi, Vacuum (Under review)

J. Zhang, S. Momota, K. Maeda, H. Terauchi, M. Furuta, T. Kawaharamura, N. Nitta, D. Wang, AIP Conf. Proc. (Accepted)

International Conference

AsiaNano 2010-Asian Conference on Nanoscience & Nanotechnology, Nov.1-3, 2010, Tokyo, Japan (poster)

E-MRS ICAM IUMRS 2011 Spring Meeting, May 9-13, 2011, Nice, France (poster)

17th International Conference on Surface Modification of Materials by Ion beams, Sept.13-17, 2011, Harbin, China (oral)

19th International conference on ion implantation technology, Jun.25-29, 2012, Valladolid, Spain (oral)

APPENDIX:

Scan electron microscopy

The working principle of SEM is the electron gun refers to the top region of the SEM that generates a beam of electrons. The electron gun produces a source of electrons (comprised of free electrons i.e. detached from the atom) and accelerates these electrons in an energy range typically 1 - 40 kV. The conventional electron gun (triode) has three components, a hot wire (called the filament or cathode [- ve] or electron emitter), a Wehnelt (grid) cap [- ve], and an anode [+ ve]. A series of electromagnetic lenses and apertures are used to reduce the diameter of the source of electrons and to place a small, focused beam of electrons (or spot) onto the specimen. The sample is produced some signals for example, secondary electron, backscattering electron, absorption electron, X ray and Auger Electron. The signal intensities depend on the surface morphology, composition of irradiated region and crystal orientation. The electron signals are amplified and processed.

For the routine scanning electron microscope images, secondary electrons (SE) form the usual image of the surface. Secondary electrons are low energy electrons formed by inelastic scattering and have energy of less than 50 eV. The low energy of these electrons allows them to be collected easily. This is achieved by placing a positively biased grill on the front of the SE detector, which is positioned off to one side of the specimen. The positive grill attracts the negative electrons and they go through it into the detector. This is the case for the Everhart-Thornley detector which is most commonly used but there is another kind of In-lens SE detector in some machines.

Backscattered (BS) electrons are high-energy electrons (> 50 eV) from the primary incident beam that are ejected back out from the samples. These BSE are used to produce a different kind of image. Such an image uses contrast to tell us about the average atomic number of the sample.

To increase the yield of SE emitted from the specimen, heavy metals such as gold or platinum are routinely used to coat specimens. An extremely thin layer is applied (~10 nm). This coating is applied for two main reasons: (1) Non conductive specimens are often coated to reduce surface charging that can block the path of SE and cause distortion of signal level and image form; and (2) Low atomic number (Z) specimens (e.g. biological samples) are coated to provide a surface layer that produces a higher SE yield than the specimen material.

Because secondary electrons have very low energies, only those produced at the surface of the sample are able to escape and be collected by the SE detector. Electrons emitted from a surface that faces away from the detector or which is blocked by the topography of the specimen, will appear darker than surfaces that face towards the detector.

Sample height, or working distance (WD), refers to the distance between the bottom of the SEM column and the top of the sample. Within the sample chamber the sample stage can be wound up closer to the end of the column (a short working distance) or dropped down lower (a long working distance). The shorter the working distance, the smaller the diameter of the beam is at the sample surface. So, when possible, the WD is kept at 10mm or smaller for high resolution imaging. The

disadvantage is that focal depth is drastically reduced at small WD. This can be offset by using a smaller objective aperture and putting up with the reduction in electrons that comes with this choice (grainier image).

In this study, we measured the morphology of irradiated Si surface and the fabricated surface crater structures by different conditions. The measurement parameters are: the accelerated voltage was 5 kV and the working distance was 8 mm.

Samples

Ion	Fluence (10^{16}/cm^2)	Energy (KeV)	Project range-R_p (nm)	Longitudinal straggling (nm)
Ar^{1+}	1	90	96.6	32.5
Ar^{1+}	2	90	96.6	32.5
Ar^{1+}	4	90	96.6	32.5
Ar^{1+}	6	90	96.6	32.5
Ar^{1+}	8	90	96.6	32.5
Ar^{4+}	0.15	80	86.6	29.7
Ar^{4+}	0.15	160	165.5	49.1
Ar^{4+}	0.15	320	332.3	81.2
Ar^{4+}	0.15	400	408.5	93.4
Ar^{4+}	1	180	185.3	53.4
Ar^{4+}	1	270	281.3	72.2
Ar^{4+}	1	360	383.2	89.5
Ar^{4+}	4	90	96.6	32.5
Ar^{4+}	4	180	281.3	72.2
Ar^{4+}	4	270	383.2	89.5